DIAGNOSTIC MODEL for BAROCLINIC, WIND-DRIVEN and TIDAL CIRCULATION in SHALLOW SEAS

Daniel R. Lynch[1], Francisco E. Werner[2], David A. Greenberg[3], John W. Loder[3]

[1]Dartmouth College, Hanover, NH USA
[2]Skidaway Institute of Oceanography, Savannah, GA USA
[3]Department of Fisheries and Oceans,
Bedford Institute of Oceanography, Dartmouth, NS CAN

October 9, 1990
Revised March 25, 1991

To Appear: *Continental Shelf Research* (JONSMOD '90)

DIAGNOSTIC MODEL for BAROCLINIC, WIND-DRIVEN and TIDAL CIRCULATION in SHALLOW SEAS

Daniel R. Lynch[1], Francisco E. Werner[2], David A. Greenberg[3], John W. Loder[3]

[1]Dartmouth College, Hanover, NH USA
[2]Skidaway Institute of Oceanography, Savannah, GA USA
[3]Department of Fisheries and Oceans,
Bedford Institute of Oceanography, Dartmouth, NS CAN

ABSTRACT

A 3-D diagnostic model for continental shelf circulation studies is presented. The model is based on the linearized hydrodynamic equations subject to surface stress, density gradient, and remote (boundary) forcing. Finite elements are used to resolve real topography. Solutions are obtained in the frequency domain, including the limit of zero frequency. A test case based on analytic solutions for tidal front circulation demonstrates the successful representation of sensitive baroclinic circulation. Representative applications to the Gulf of Maine region, including the Bay of Fundy, Georges Bank, and a portion of the Scotian Shelf, are shown for wind, alongshelf transport, and tidal front circulation on Georges Bank.

INTRODUCTION

In a series of previous papers we have explored aspects of 3-D continental shelf modeling using the finite element method (FEM) in order to obtain topographic resolution at reasonable levels of discretization. In Lynch and Officer (1985; herein LO85) we present analytic solutions to the linearized harmonic equations and introduce an exact decoupling strategy among horizontal and vertical modes which maintains the dependence of bottom stress on bottom velocity. In Lynch and Werner (1987; herein LW87) this strategy was used with horizontal finite elements along with either analytic or FEM treatment of the vertical. Therein, the 3-D FEM problem is reduced by the decoupling to sequential solutions of a 2-D horizontal problem with conventional sparse, banded FEM matrix; and a simple 1-D problem with tridiagonal matrix. As a result the 3-D problem scales effectively as a 2-D FEM problem, without further simplifying the linearized equations. In Lynch and Werner (1990; herein LW90) this same structure is exploited for more general time-stepping problems, wherein semi-implicit calculations in each time step share the same sequential 2-D/1-D structure without simplifying the nonlinear 3-D equations.

The present paper addresses the linearized harmonic problem. In LW87 we concentrated on tides and wind; here we extend the scope to that of a general diagnostic tool. Specifically, we provide for a baroclinic pressure gradient; add a new boundary condition for geostrophically balanced along-shelf flow; and include the computation of the vertical velocity. We retain the general harmonic formulation, although the examples here emphasize steady-state phenomena. We introduce an analytic test case for baroclinic verification; and demonstrate a range of phenomena in the Gulf of Maine region.

Recent 3-D linearized diagnostic studies of coastal areas can be found in Askari et al. (1989) and Hukuda et al. (1989). These 2 studies are related, in spirit, to the formulation developed herein, although neither allows imposition of a general three-dimensional density field.

THEORY

We solve the linearized 3-D shallow water equations with conventional hydrostatic and Boussinesq assumptions, and eddy viscosity closure in the vertical. The density field is presumed known and constitutes a fixed baroclinic pressure gradient. The response (3-D velocity field plus barotropic pressure) to this forcing, combined with wind and barotropic forcing at open water boundaries, is sought on detailed topography. For generality and for compatibility with previous model development (LW87) we assume periodic-in-time solutions of the form $q(\mathbf{x},t) = Re(Q(\mathbf{x})e^{j\omega t})$, with Q the complex amplitude of q and ω the frequency. The steady responses are simply the limiting case $\omega = 0$.

The horizontal momentum equation is

$$j\omega\mathbf{V} + \mathbf{f} \times \mathbf{V} - \frac{\partial}{\partial z}\left(N\frac{\partial \mathbf{V}}{\partial z}\right) = \mathbf{G} + \mathbf{R} \tag{1}$$

$$N\frac{\partial \mathbf{V}}{\partial z} = h\mathbf{\Psi} \qquad (z = 0) \tag{2}$$

$$N\frac{\partial \mathbf{V}}{\partial z} = k\mathbf{V} \qquad (z = -h) \tag{3}$$

in which

$\mathbf{R}(x,y,z) \equiv -\frac{g}{\rho_0}\int_z^0 \nabla\rho dz$ is the baroclinic pressure gradient, assumed known
$\mathbf{G}(x,y) \equiv -g\nabla\zeta$ is the barotropic pressure gradient, assumed unknown
$\rho(x,y,z,t)$ is the fluid density
$\zeta(x,y)$ is the free surface elevation
$\mathbf{V}(x,y,z)$ is the horizontal velocity
$W(x,y,z)$ is the vertical velocity
ω is the radian frequency
j is the imaginary unit, $\sqrt{-1}$
$h(x,y)$ is the bathymetric depth
$\mathbf{f} \equiv f\hat{\mathbf{z}}$ is the Coriolis vector
$N(x,y,z)$ is the vertical eddy viscosity
g is gravity
(x,y) are the horizontal coordinates
z is the vertical coordinate, positive upward.
∇ is the *horizontal* gradient $(\partial/\partial x,\ \partial/\partial y)$
$h\mathbf{\Psi}(x,y)$ is the atmospheric forcing
k is a linear bottom stress coefficient.

(Note that $z = 0$ at the undisturbed free surface; and $z = -h$ at the bottom.) All hydrodynamic variables are represented as complex amplitudes of time-periodic motions; and throughout we indicate by an overbar the vertical average of any quantity. The vertical average of (1) is

$$j\omega\bar{\mathbf{V}} + \mathbf{f}\times\bar{\mathbf{V}} + \frac{k}{h}\mathbf{V}(-h) = \mathbf{G} + \mathbf{\Psi} + \bar{\mathbf{R}} \tag{4}$$

In addition we have the continuity equation

$$\frac{\partial W}{\partial z} + \nabla\cdot\mathbf{V} = 0 \tag{5}$$

and its vertical average

$$j\omega\zeta + \nabla\cdot(h\bar{\mathbf{V}}) = 0 \tag{6}$$

We record also the weak form of (6):

$$\langle j\omega\zeta\,\phi_i\rangle - \langle h\bar{\mathbf{V}}\cdot\nabla\phi_i\rangle = -\oint h\bar{\mathbf{V}}\cdot\hat{\mathbf{n}}\phi_i\,ds \tag{7}$$

where $\langle\,\rangle$ is a domain integral over (x, y); $\oint ds$ is the enclosing boundary integral; $\hat{\mathbf{n}}$ is the unit normal, directed outward; and $\phi_i(x, y)$ is an arbitrary weighting function. Note that conventional horizontal boundary conditions will be enforced on either ζ or $h\bar{\mathbf{V}} \cdot \hat{\mathbf{n}}$ to close the boundary-value problem.

The momentum equation is simplified by introduction of the surrogate velocity variables

$$\nu^+ = \frac{V_x + jV_y}{2}; \qquad \nu^- = \frac{V_x - jV_y}{2} \tag{8}$$

$$V_x = \nu^+ + \nu^-; \qquad jV_y = \nu^+ - \nu^-. \tag{9}$$

which removes the Coriolis coupling:

$$j(\omega \pm f)\nu^\pm - \frac{\partial}{\partial z}\left(N\frac{\partial \nu^\pm}{\partial z}\right) = G^\pm + R^\pm \tag{10}$$

$$N\frac{\partial \nu^\pm}{\partial z} = h\psi^\pm \qquad (z = 0) \tag{11}$$

$$N\frac{\partial \nu^\pm}{\partial z} = k\nu^\pm \qquad (z = -h) \tag{12}$$

with forcing terms defined as

$$G^\pm = \frac{G_x \pm jG_y}{2} \tag{13}$$

$$\psi^\pm = \frac{\psi_x \pm j\psi_y}{2} \tag{14}$$

$$R^\pm = \frac{R_x \pm jR_y}{2} \tag{15}$$

By inspection, the solution to (10-12) can be written as

$$\nu^\pm(z) = G^\pm P_1^\pm(z) + \psi^\pm P_2^\pm(z) + P_3^\pm(z) \tag{16}$$

where the functions $P_i^\pm$ each satisfy the simple diffusion equation (10), forced as follows:*

$$P_1^\pm : G = 1; \psi = 0; R = 0.$$

$$P_2^\pm : G = 0; \psi = 1; R = 0.$$

---

* The distinction between P_2 and P_3 is maintained here for its interpretive content; but is not necessary. The merger of P_2 into P_3, by the alternate definition ($P_3^\pm : G = 0; \psi = \psi^\pm; R = R^\pm$) allows use of all the formulae below with the simplification $P_2^\pm = 0$ everywhere.

$$P_3^{\pm} : G = 0; \psi = 0; R = R^{\pm} \tag{17}$$

Recovery of $\mathbf{V}$ from $\nu^{\pm}$ is then straightforward, using (9):

$$\begin{aligned}\mathbf{V}(z) = \mathbf{G}\left(\frac{P_1^+ + P_1^-}{2}\right) - j\left(\frac{P_1^+ - P_1^-}{2}\right)\hat{\mathbf{z}} \times \mathbf{G} \\ +\mathbf{\Psi}\left(\frac{P_2^+ + P_2^-}{2}\right) - j\left(\frac{P_2^+ - P_2^-}{2}\right)\hat{\mathbf{z}} \times \mathbf{\Psi} \\ +\hat{\mathbf{x}}\left(P_3^+ + P_3^-\right) - j\hat{\mathbf{y}}\left(P_3^+ - P_3^-\right)\end{aligned} \tag{18}$$

expressing a superposition of responses to barotropic, wind, and density gradient forcing. Note that the six functions $P_i^{\pm}$ can be obtained independently at any horizontal position by any of several methods for solving the 1-D diffusion equation.

The unknown barotropic pressure gradient $\mathbf{G} \equiv -g\nabla\zeta$ in (18) is determined by application of the vertically averaged continuity equation (6). Substitution of (18) into (6) or its weak form (7) eliminates $\bar{\mathbf{V}}$ and produces a scalar Helmholtz-like equation in ζ alone. The resulting weak form is

$$\begin{aligned}\langle j\omega\zeta\,\phi_i\rangle + \left\langle \left[\left(\frac{\bar{P}_1^+ + \bar{P}_1^-}{2}\right)gh\nabla\zeta - j\left(\frac{\bar{P}_1^+ - \bar{P}_1^-}{2}\right)\hat{\mathbf{z}} \times gh\nabla\zeta\right] \cdot \nabla\phi_i \right\rangle = \\ -\oint h\bar{\mathbf{V}} \cdot \hat{\mathrm{n}}\phi_i\,ds + \left\langle \left[\left(\frac{\bar{P}_2^+ + \bar{P}_2^-}{2}\right)h\mathbf{\Psi} - j\left(\frac{\bar{P}_2^+ - \bar{P}_2^-}{2}\right)\hat{\mathbf{z}} \times h\mathbf{\Psi}\right] \cdot \nabla\phi_i \right\rangle \\ +\left\langle \left[\left(\bar{P}_3^+ + \bar{P}_3^-\right)h\hat{\mathbf{x}} - j\left(\bar{P}_3^+ - \bar{P}_3^-\right)h\hat{\mathbf{y}}\right] \cdot \nabla\phi_i \right\rangle\end{aligned} \tag{19}$$

This 2-D, horizontal equation is especially amenable to Galerkin finite element solution on simple linear triangular elements. Its solution provides the barotropic pressure response which accompanies the imposed wind, density field, and open-water barotropic boundary conditions.

Integration of (10) from $z = -h$ to $z = 0$, and use of (11,12), provides a useful relation between $\bar{\nu}^{\pm}$ and $\nu^{\pm}(-h)$:

$$j(\omega \pm f)\bar{\nu}^{\pm} - \psi^{\pm} + \frac{k}{h}\nu^{\pm}(-h) = \bar{G}^{\pm} + \bar{R}^{\pm} \tag{20}$$

(Recall that an overbar indicates a vertically averaged quantity.) As in LW87, we find for the various $P_i(z)$:

$$\bar{P}_{1,2}^{\pm} = \frac{1}{j(\omega \pm f)}\left[1 - \frac{k}{h}P_{1,2}^{\pm}(-h)\right] \tag{21}$$

$$\bar{P}_3^{\pm} = \frac{1}{j(\omega \pm f)}\left[\bar{R}^{\pm} - \frac{k}{h}P_3^{\pm}(-h)\right] \tag{22}$$

which may be used to avoid the calculation of the vertical averages.**

An alternate route to an equivalent statement of the horizontal problem is available following LW87. This approach takes advantage of the fact that the bottom stress may be expressed in terms of $\bar{\mathbf{V}}$, reducing the vertically averaged momentum equation to an equivalent 2-D form. First, $G^{\pm}$ can be eliminated from (16) by use of its vertical average:

$$G^{\pm} = \frac{1}{\bar{P}_1^{\pm}}\left[\bar{\nu}^{\pm} - \psi^{\pm}\bar{P}_2^{\pm} - \bar{P}_3^{\pm}\right] \tag{23}$$

and therefore

$$\nu^{\pm}(z) = \left(\frac{P_1(z)}{\bar{P}_1}\right)^{\pm}\bar{\nu}^{\pm} + \left(P_2(z) - P_1(z)\frac{\bar{P}_2}{\bar{P}_1}\right)^{\pm}\psi^{\pm} + \left(P_3(z) - P_1(z)\frac{\bar{P}_3}{\bar{P}_1}\right)^{\pm}. \tag{24}$$

It follows that

$$k\nu^{\pm}(-h) = \tau^{\pm}h\bar{\nu}^{\pm} - \alpha^{\pm}h\psi^{\pm} - \beta^{\pm}h \tag{25}$$

with

$$\tau^{\pm} \equiv \frac{kP_1^{\pm}(-h)}{h\bar{P}_1^{\pm}} \tag{26}$$

$$\alpha^{\pm} \equiv \tau^{\pm}\bar{P}_2^{\pm} - \frac{k}{h}P_2^{\pm}(-h) \tag{27}$$

$$\beta^{\pm} \equiv \tau^{\pm}\bar{P}_3^{\pm} - \frac{k}{h}P_3^{\pm}(-h) \tag{28}$$

Recovery of the bottom stress in the original (x, y) system, via (9), yields

$$\begin{aligned} k\mathbf{V}(-h) = {} & \left(\frac{\tau^{+} + \tau^{-}}{2}\right)h\bar{\mathbf{V}} - j\left(\frac{\tau^{+} - \tau^{-}}{2}\right)\hat{\mathbf{z}} \times h\bar{\mathbf{V}} \\ & - \left(\frac{\alpha^{+} + \alpha^{-}}{2}\right)h\mathbf{\Psi} + j\left(\frac{\alpha^{+} - \alpha^{-}}{2}\right)\hat{\mathbf{z}} \times h\mathbf{\Psi} \\ & - \left(\beta^{+} + \beta^{-}\right)h\hat{\mathbf{x}} + j\left(\beta^{+} - \beta^{-}\right)h\hat{\mathbf{y}} \end{aligned} \tag{29}$$

Finally, use of (29) in (4) to eliminate the bottom velocity gives the equivalent 2-D system

$$j\omega\bar{\mathbf{V}} + \mathbf{f}' \times \bar{\mathbf{V}} + \tau'\bar{\mathbf{V}} = \mathbf{G} + \mathbf{\Psi}' + \bar{\mathbf{R}}' \tag{30}$$

** If as suggested above P_2 and P_3 are merged, replace $\bar{R}^{\pm}$ with $\bar{R}^{\pm} + \psi^{\pm}$ in (22) where the prime quantities $\mathbf{f}'$, τ', $\mathbf{\Psi}'$ and $\bar{\mathbf{R}}'$ all contain contributions from the bottom stress:

$$\mathbf{f}' = \mathbf{f} - j\left(\frac{\tau^+ - \tau^-}{2}\right)\hat{\mathbf{z}} \tag{31}$$

$$\tau' = \frac{\tau^+ + \tau^-}{2} \tag{32}$$

$$\mathbf{\Psi}' = \mathbf{\Psi}\left[1 + \left(\frac{\alpha^+ + \alpha^-}{2}\right)\right] - j\left(\frac{\alpha^+ - \alpha^-}{2}\right)\hat{\mathbf{z}} \times \mathbf{\Psi} \tag{33}$$

$$\bar{\mathbf{R}}' = \bar{\mathbf{R}} + \hat{\mathbf{x}}(\beta^+ + \beta^-) - j\hat{\mathbf{y}}(\beta^+ - \beta^-) \tag{34}$$

As in LW87, $\tau^\pm$, $\alpha^\pm$ and $\beta^\pm$ depend on $\omega \pm f$, $N(z)$, h, and k and thus vary with frequency as well as (x, y); and all of the vertical detail is embodied without loss of information in the parameters $\mathbf{f}'$, τ', $\mathbf{\Psi}'$, and $\bar{\mathbf{R}}'$. This 2-D system permits the classical expression of $\bar{\mathbf{V}}$ in terms of the gravity, wind, and baroclinic forcing:

$$\bar{\mathbf{V}} = \left(\frac{(j\omega + \tau')(\mathbf{G} + \mathbf{\Psi}' + \bar{\mathbf{R}}') - \mathbf{f}' \times (\mathbf{G} + \mathbf{\Psi}' + \bar{\mathbf{R}}')}{(j\omega + \tau')^2 + f'^2}\right) \tag{35}$$

This may in turn be substituted into the vertically integrated continuity equation to produce a Helmholtz equation equivalent to (19):

$$\langle j\omega\zeta\, \phi_i\rangle + \left\langle\left[\frac{(j\omega + \tau')gh\nabla\zeta - \mathbf{f}' \times gh\nabla\zeta}{(j\omega + \tau')^2 + f'^2}\right] \cdot \nabla\phi_i\right\rangle =$$

$$-\oint h\bar{\mathbf{V}} \cdot \hat{\mathbf{n}}\phi_i\, ds + \left\langle\left[\frac{(j\omega + \tau')h(\mathbf{\Psi}' + \bar{\mathbf{R}}') - \mathbf{f}' \times h(\mathbf{\Psi}' + \bar{\mathbf{R}}')}{(j\omega + \tau')^2 + f'^2}\right] \cdot \nabla\phi_i\right\rangle \tag{36}$$

Like (19), this equation allows computation of ζ as a scalar, 2-D problem subject to barotropic boundary conditions. While the derivation of (36) is more circuitous, it provides a simple set of recipes for converting /upgrading any 2-D shallow water solver based on the linearized harmonic equations to the present 3-D diagnostic level. In addition the equivalent 2-D momentum equation (30) provides some insight in the departure of the prime quantities from their conventional 2-D forms, which is not readily obtained from the more direct form (19).

SOLUTION PROCEDURE

The numerical solution is implemented in four sequential steps, using a finite element mesh of linear triangles in the horizontal:

1) The vertical structure is computed in terms of τ', f', $\mathbf{\Psi}'$ and $\bar{\mathbf{R}}'$ at each node. The six solutions $P^{\pm}_{1,2,3}$ are computed under each node – each requires solution of a 1-D diffusion equation, which we solve by the Galerkin method on 1-D linear finite elements. Because

these are tridiagonal systems, they are not a limiting factor in the overall computational method.

2) The surface elevation is obtained by the Galerkin method on the horizontal grid of triangles. Expanding the solution in terms of unknown nodal values ζ_j and the triangular basis functions ϕ_j:

$$\zeta(x,y) = \sum_j \zeta_j \phi_j(x,y) \tag{37}$$

we obtain from (36) the matrix equation

$$\begin{aligned}
[A]\{\zeta\} &= \{B\} - \{F\} \\
A_{ij} &= \langle j\omega\phi_j\phi_i \rangle + \left\langle \left[\frac{(j\omega + \tau')gh\nabla\phi_j - \mathbf{f}' \times gh\nabla\phi_j}{(j\omega+\tau')^2 + f'^2} \right] \cdot \nabla\phi_i \right\rangle \\
B_i &= \left\langle \left[\frac{(j\omega + \tau')h(\mathbf{\Psi}' + \bar{\mathbf{R}}') - \mathbf{f}' \times h(\mathbf{\Psi}' + \bar{\mathbf{R}}')}{(j\omega+\tau')^2 + f'^2} \right] \cdot \nabla\phi_i \right\rangle \\
F_i &= \oint h\bar{\mathbf{V}} \cdot \hat{\mathbf{n}}\phi_i \, ds
\end{aligned} \tag{38}$$

In the present implementation (Lynch 1990) all inner products are evaluated numerically, with quadrature points at the nodes of the triangles. Barotropic BC's are enforced on this system in any of three ways:

Type I: Elevation known. In this case the Galerkin equation weighted by ϕ_i is removed in favor of exact specification of ζ_i.

Type II: $\bar{\mathbf{V}} \cdot \hat{\mathbf{n}}$ known. In this case the boundary transport integral F_i is evaluated from the given BC.

Type III: Geostrophically balanced transport. In this case neither elevation nor transport are known, but a geostrophic balance is assumed between them:

$$h\bar{\mathbf{V}} \cdot \hat{\mathbf{n}} = \frac{h}{f}(\mathbf{G} + \mathbf{\Psi}' + \bar{\mathbf{R}}') \cdot \hat{\mathbf{s}} \tag{39}$$

where $\hat{\mathbf{s}}$ is the local tangential direction. (Essentially we assume $h\bar{\mathbf{V}} \cdot \hat{\mathbf{s}} = 0$.) This relation is substituted into the transport integral F_i; the known parts $(\mathbf{\Psi}' + \bar{\mathbf{R}}') \cdot \hat{\mathbf{s}}$ are moved into B_i; the unknown part $\mathbf{G} \cdot \hat{\mathbf{s}} \equiv -g \sum \zeta_j \frac{\partial \phi_j}{\partial s}$ is moved to the left-side and embedded in the matrix $[A]$:

$$\begin{aligned}
A'_{ij} &= A_{ij} - \int \frac{gh}{f} \frac{\partial \phi_j}{\partial s} \phi_i \, ds \\
B'_{ij} &= B_{ij} - \int \frac{h}{f}(\mathbf{\Psi}' + \bar{\mathbf{R}}') \cdot \hat{\mathbf{s}}\, \phi_i \, ds
\end{aligned} \tag{40}$$

with $\int ds$ indicating integration over the Type III boundary only.

3) Velocity profiles. Once ζ is available, we differentiate it numerically to obtain nodal values of **G** by a Galerkin approximation:

$$\sum_j \langle \phi_i \phi_j \rangle \mathbf{G_j} = -\langle g \nabla \zeta \phi_i \rangle \tag{41}$$

Nodal quadrature reduces the mass matrix $\langle \phi_i \phi_j \rangle$ to a diagonal matrix, greatly simplifying this calculation. Once the $\mathbf{G}_i$ are computed, the velocity profiles are either assembled from memory according to (18); or recomputed by a single tridiagonal calculation under each horizontal node.

4) Vertical velocities. Finally, we compute the vertical velocities at every node from the continuity equation (5). To do so requires construction of a 3-D FE mesh in order to differentiate $\mathbf{V}(x, y, z)$, and we follow exactly the procedure given in LW90. The horizontal mesh is projected downward in perfectly vertical lines and each is discretized into the same number of vertical elements. These are then connected horizontally in the identical topology as the original 2-D mesh, thereby filling the volume with 6-node linear elements. Effectively, this creates an (x, y, σ) coordinate system. Unless otherwise stated, the simulations here employ uniform relative vertical mesh spacing everywhere, i.e. uniform $\Delta\sigma$.

BAROCLINIC TEST CASE

Extensive testing of the tidal and wind-driven aspects of this model has been reported previously (LW87), against analytic solutions. Here we add an analytic test of the baroclinic response. The test consists of an idealized 2-D tidal front in a stratified shallow sea, with density field prescribed as

$$\frac{\partial \rho}{\partial x} = \frac{1}{2}\frac{\partial \Delta\rho(x)}{\partial x}(s - cos(\pi z/h(x))) \tag{42}$$

$$\Delta\rho(x) = \Delta\rho_s, \quad x \leq 0$$

$$\Delta\rho(x) = \frac{1}{2}\Delta\rho_s(1 + cos(\pi x/L)), \ 0 \leq x \leq L \tag{43}$$

$$\Delta\rho(x) = 0, \quad x \geq L$$

h is the bathymetric depth; $\Delta\rho_s$ is the surface-to-bottom density difference in the stratified region; and s is an adjustable parameter which, for uniform h, sets the cross-front gradient in depth-averaged density as illustrated in figure 1a. This case was introduced by Loder (1980) wherein exact solutions for $U(x,z)$ and $V(x,z)$ are presented under the conditions of zero depth-integrated cross-front transport and vertically uniform N. As discussed in Garrett and Loder (1981), these solutions show a sensitivity to vertical viscosity which is of considerable practical importance. As a result they constitute a useful test problem.

We solve this problem on the mesh depicted in figure 1b, with uniform h, N, k, and Δz. Density is prescribed at the mesh nodes and differentiated numerically. The barotropic boundary conditions indicated include the requirement of periodicity at the ends of the mesh, where no other boundary condition is enforced. As in Garrett and Loder (1981) we normalize the velocity results by $-\frac{1}{2}\frac{gh}{\rho_o f}\frac{\partial\Delta\rho}{\partial x}$. (This along-front speed would be achieved at the surface for the $s = 1$, inviscid case.) The analytic solution then depends uniquely on the dimensionless parameters s, $E \equiv \frac{N}{fh^2}$, and $\lambda \equiv \frac{N}{kh}$. Figures 2 through 6 compare analytic and numerical velocities sampled at the center of the mesh, with $s = 0$ and $\lambda = \sqrt{E}$, for the range of E considered in Garrett and Loder (1981). (Their figure 5.) The dimensional parameters for these runs were $g = 9.806$, $f = .9946 \times 10^{-4}$, $h = 95.$, $\omega = 10^{-12}$, $L = 25 \times 10^3$, and $\Delta\rho_s = 1.2$, all in MKS units.

Figure 2 displays results for intermediate E. The agreement is clear and satisfying. Relative to vertical resoultion, we found previously (LW87) a useful rule of thumb to be 3 to 10 Δz per Ekman depth $\delta = \sqrt{2N/f}$. The case shown in figure 2 is at the threshold of this range – 20 equally-spaced vertical elements gives 2.8 Δz per δ, confirming that rule of thumb.

Vertically averaging the steady along-front momentum equation provides the useful relation

$$f\bar{U} + g\frac{\partial \zeta}{\partial y} + \frac{k}{h}V_b = \bar{R}_y \tag{44}$$

where V_b is the along-front bottom velocity. In the analytic case, it is assumed that $\frac{\partial\zeta}{\partial y} = 0$; and $\frac{\partial\zeta}{\partial x}$ is determined a priori such that the cross-front transport $\bar{U}$ also vanishes. With $\bar{R}_y = 0$ this leads to the interesting analytic property $V = \frac{\partial V}{\partial z} = 0$ at the bottom. In the numerical solution however, $\frac{\partial\zeta}{\partial y} = 0$ exactly only along one boundary, and weakly along the periodic boundaries, leaving internal deviations free to develop. Similarly, the cross-front transport is required to vanish only along one boundary, and no constraints are enforced directly on $\frac{\partial\zeta}{\partial x}$. Nevertheless, in Figure 2 both analytic bottom properties $V = 0$ and $\frac{\partial V}{\partial z} = 0$ are reproduced nicely.

In figure 3, E is reduced by a factor of 10 with the same vertical resolution, giving only .89 Δz per δ. The degradation in accuracy in the bottom boundary layer is apparent, although the overall solution is not damaged significantly. (Note that the baroclinic forcing is well-resolved with 20 vertical elements.) Enhanced resolution restores the accuracy at the bottom - e.g. in Figure 4 we use 100 elements in the vertical, giving 4.5 Δz per δ.

The effect of increasing the viscosity is shown in Figure 5. Here we find an error in the along-front velocity which is nearly uniform with depth; it is the dominant error in a generally small velocity field. In this case, 20 vertical elements overresolves the Ekman depth, 8.9 Δz per δ, and further vertical mesh refinement produces no change in the error. The horizontal discretization controls this error, which arises in the cross-front barotropic presure gradient. In Figure 6 we show the effect of halving the horizontal mesh size (four times as many nodes), which restores satisfying accuracy.

These solutions, along with those for other values of s (Garrett and Loder, 1981) imply a double-cell circulation on cross-front (x, z) transects, illustrated in figure 7, which is sensitive to E and the density field. To illustrate the practical significance of this sensitivity, we introduce an idealized bank topography across the x-axis of the mesh, keeping N and k constant and imposing the analytic density gradient (42,43) at nodes (with $h = h(x)$). The resulting circulation in figure 8 shows the lower cell penetrating the surface on the shallow side of the front. The primary features - convergence of cross-front surface velocities and uniformly shoalward bottom flow - are reminiscent of those displayed in Garrett and Loder (1981, figure 10) and observed at tidal fronts (Simpson 1981, figure 3). ***

*** Note that in figures 7 and 8, vectors are drawn originating at the nodes, which are marked. The marker on each vector thus indicates its *tail* and its location.

EXAMPLE APPLICATIONS: THE GULF OF MAINE

As representative applications, we consider the Gulf of Maine region, depicted in figure 9. These waters exhibit several well-documented oceanographic features, including strong barotropic and baroclinic circulation around Georges Bank. A comprehensive review of the regional oceanography is available in Backus (1987); a review of previous numerical modeling efforts is available in Greenberg (1991).

The horizontal finite element mesh appears in figure 10. There are 3156 nodes and 5558 triangular elements. This mesh was derived from the original Greenberg (1979) topography, enhancing the geometric realism at shoreline boundaries and maintaining the original open boundary resolution. On the interior, uniform discretization of the barotropic radius of deformation is achieved on the variable topography by maintaining spatially uniform $\sqrt{gh}/f\Delta x$ (Henry, 1988). As a result, available detail is concentrated in shallow and shoreline areas.

On this mesh we have computed three illustrative steady-state solutions, representing the separate effects of a) barotropic inflow across the Scotian Shelf, b) along-shelf wind stress, and c) summertime density structure on Georges Bank. Boundary conditions for these are as follows: across the Scotian Shelf we specify the surface elevation; along the open ocean we maintain constant elevation (note that most of this boundary approximates the 200 meter isobath); and across the New England shelf flow is allowed to enter or exit geostrophically. In each case, 10 uniform vertical elements are used throughout, with constant $(N,k) = (.02, .005)$ in MKS units. The limit of effectively zero frequency is realized at $\omega = 10^{-12} sec^{-1}$. All calculations are made on an f-plane, at 43.5° North.

As a first example, we show the isolated influence of along-shelf barotropic transport originating on the Scotian Shelf, with no wind and constant density. This solution is driven as in Wright et al (1986) by specifying a barotropic setup across the Scotian Shelf: $\zeta = 0.1\,m$ at the coast, decaying exponentially across the shelf with a length scale of $39\,km$. This approximates the wintertime geostrophic transport estimated by Drinkwater et al (1979) for the Halifax section. In figure 11, the solution for ζ is plotted, and plots for vertically averaged and bottom velocity appear in figure 12. The flow into the Gulf of Maine from the Scotian Shelf largely follows the topography, including counterclockwise flows around Jordan and Georges Basins. The western limb of the Georges Basin flow impinges on the northern flank of Georges Bank and splits, with one branch circulating clockwise around the Bank and ultimately exiting through Northeast Channel, and the other exiting directly through Great South Channel. Overall, the vertically averaged solution strongly resembles the 2-D response obtained by Wright et al (1986): transports through the Northeast Channel and across Nantucket Shoals are 2.95×10^5 and $1.40 \times 10^5\ m^3/s$, respectively, compared with 2.8×10^5 and $1.4 \times 10^5\ m^3/s$ in Wright et al.

Owing to the strictly barotropic forcing, the velocity profiles show little departure from their vertical averages, except for a counterclockwise (downgradient) veering in the bottom Ekman layer (figure 12b). This generally gives the bottom flow a downslope component, such as along the Nova Scotia coast and around most of Georges Bank. The surface velocity pattern is indistinguishable from the vertically averaged pattern in figure 12a.

As a second example, we have computed the response to a uniform wind stress from the southwest, the prevailing direction in summer. As in Wright et al (1986) we specify a corresponding barotropic setdown across the Scotian Shelf to represent the effect of wind stress forcing on the unmodelled eastern part of the Scotian Shelf. In detail, the wind stress is $0.1\,Pa$ everywhere, directed "along-shelf" i.e. perpendicular to the two parallel cross-shelf boundaries; the setdown is $0.1\,m$ at the Nova Scotia coast with a $39\,km$ cross-shelf exponential decay scale; and density is uniform. The vertically averaged solution (figure 13a) again shows strong similarity to the 2-D response obtained by Wright et al (1986), with a general along-shelf flow structured by topography and the coastline. The cross-shelf circulation includes vertically averaged flows into the Gulf through Northeast and Great South Channels, which converge along the northern flank of Georges Bank and produce a flow onto and over the Bank. Gulf outflow occurs on and north of Browns Bank. The Northeast Channel inflow is qualitatively consistent with the observed influence of along-shelf wind stress (Ramp et al, 1985; Smith 1989; Brooks 1991), although it appears that improved topographic resolution and baroclinic dynamics are required to produce the detailed response. Transports through the Northeast Channel and across Nantucket Shoals are 5.95×10^5 and 4.18×10^5 m^3/s, respectively, compared with 5.2×10^5 and 4.5×10^5 m^3/s in Wright et al.

The wind-driven velocities show considerable vertical structure. At the surface (figure 13b), the flow is almost uniformly eastward as expected for the surface Ekman layer, with notable perturbations near coastal boundaries, on the northern flank of Georges Bank, and in Northeast and Great South Channels where there are strong additional flow contributions associated with the pressure field. The bottom velocities (figure 13c) generally mimic the vertically averaged pattern, except for some relative strengthening of the flow on central Georges Bank and a general counterclockwise veering, again as expected for the bottom Ekman layer. The latter results in a pronounced onshore bottom flow along the Nova Scotia and Maine coasts as part of a classical wind-driven coastal upwelling, consistent with observational suggestions (Petrie et al 1987; Brooks and Townsend 1989) of a contribution to reduced coastal surface temperature in summer from this process. Overall, this solution provides further support for along-shelf wind stress having a significant influence on low-frequency circulation in the Gulf.

Finally, we consider the circulation driven by a representative summer density distribution on Georges Bank. During summer, intense vertical mixing on the Bank maintains well-mixed conditions there (e.g. Garrett et al 1978), while stratified conditions prevail in the surrounding waters. As a result, a seasonal tidal front circumscribes the bank (e.g. Loder and Wright 1985). Here we show the circulation driven by a composite density field on Georges Bank, with no wind stress and with elevation on the Scotian Shelf boundary clamped at zero.

The density field was based on monthly-mean values provided by the Marine Environmental Data Service (Department of Fisheries and Oceans, Ottawa, Canada) for specified depths in 30 polygons over the Bank. (See figure 14.) The monthly means were based on all available data through 1987 (about 650 profiles for July – September), and were subsequently averaged to obtain means for the three-month summer period. The depths were at $10\,m$ intervals between 0 and $50\,m$, and at 75 and $100\,m$. The shape and size of the polygons were specified with consideration to minimizing spatial structure in the topography (and density) within each. A few inversions in the density profiles were removed and replaced using vertical interpolation or extrapolation.

The vertical structure of the resulting density field is illustrated in figure 15, which shows a north-south section near $67^o\,W$. A vertically well-mixed zone over the Bank and tidal fronts with strong cross-bank gradients over the Bank's sides are apparent. The horizontal structure of the field is illustrated in figure 16 which shows the density difference between the surface and $50\,m$ (or bottom in shallower areas). The tidal front can be seen to extend around the Bank, in general agreement with predictions of Simpson and Hunter's (1974) depth/dissipation criterion (Loder and Greenberg 1986). The dominant feature of the associated geostrophic shear (dynamic height) in the upper $40\,m$ (not shown) is a contribution to the summertime intensification of the clockwise gyre around the Bank (e.g. Butman et al 1987). Additionally, the dynamic height exhibits a local maximum on the southwest end of the bank and a local minimum on the northeast end, suggesting closed secondary circulations at those locations. Overall, this density field includes the primary features of the known frontal structure over the Bank, although the results below indicate that additional data are required, particularly over the Bank's sides.

This density field was interpolated from the polygon centroids onto the horizontal finite element mesh, for each of the eight level surfaces. Outside of the polygons and/or beyond the $150\,m$ isobath, a uniform stratification was prescribed, equal to the average of the polygons on the edge of the data. The finite element density fields were then individually differentiated on the level surfaces by a Galerkin procedure, to produce nodal values of density gradient. Finally, these nodal gradients on the eight levels were interpolated onto the vertical node structure of the FE mesh. The resulting circulation is thus driven primarily by the frontal structure in isolation.

In figure 17 we show the resulting circulation. The elevation (figure 17a) generally imitates the dynamic height, including the local extrema on the two ends of the bank. The surface velocity (figure 17b) shows a strong clockwise circulation, of order $10 - 20\,cm/s$, in qualitative agreement with the observed intensification of the gyre in summer. The flow on the northern flank is intensely confined by the steep topography, and that on the southern flank is more diffuse, again in qualitative agreement with previous studies. The two secondary circulation cells evident in the elevation field are clearly visible, as are smaller, spurious peripheral circulations corresponding to the unphysical truncation of the density field. Along the northern flank, there are mesh-scale perturbations which become more pronounced at depth. These are the result of imperfect representation of the steep topography there, combined with the even coarser resolution of the density field both across and along the northern flank.

These circulation patterns invite hypotheses with implications for the ecology of the Bank, which must await a complete sensitivity study relative to forcing, boundary conditions, vertical mixing, and spatial resolution.

DISCUSSION

The value of a diagnostic computation lies in the balance between reduced physics and reduced computational burden. On the physical side, it is crucial to capture as many of the first-order effects of large-scale 3-D flows over topography as possible. We find the marriage of the geometrically flexible FEM with the linearized equations provides useful diagnostic insight, particularly as a prelude to more comprehensive nonlinear simulation. On the cost-effectiveness side of the balance, the present 3-D algorithm scales effectively as a 2-D FEM problem, which can be accomodated readily on affordable workstations.

The Gulf of Maine results shown here are strictly exploratory. We are presently examining their sensitivity to topographic resolution, open boundary location and conditions, vertical mixing parameters, etc, (see e.g. Hukuda et al 1989) and quantifying the nonlinear imbalances implied by our linearized solutions. Particularly in 3-D, it is crucial to establish this basic understanding prior to full, nonlinear simulation of all effects coupled.

ACKNOWLEDGMENTS

This work was supported by the US National Science Foundation, Grants OCE-9012612 and OCE-9018388; by the University of New Hampshire Seagrant Program, Grant R/FMD-110; and by the Canadian Federal Interdepartmental Panel on Energy, Research, and Development. We thank W.S. Brown for many helpful discussions concerning the Gulf of Maine circulation.

REFERENCES

Askari, F., L.J. Pietrafesa and G.S. Janowitz. Steady, three-dimensional circulation on a cuspate continental shelf. *Continental Shelf Research*, **9**, 497-526 (1989).

Backus, R.H., editor. *Georges Bank*, MIT Press, 1987 (593 pp).

Brooks, D.A. Currents at Lindenkohl Sill in the southern Gulf of Maine. *J. Geophysical Res.* (in press 1991).

Brooks, D.A. and D.W. Townsend. Variability of the coastal current and nutrient pathways in the eastern Gulf of Maine. *J. Mar. Res.* **47**, 303-321 (1989).

Butman, B., J.W. Loder, and R.C. Beardsley. The seasonal mean circulation on Georges Bank: observation and theory. In R.H. Backus, ed.: *Georges Bank*, MIT Press, pp 125-138 (1987).

Drinkwater, K., B. Petrie, W.H. Sutcliffe, Jr. Seasonal geostrophic transports along the Scotian Shelf. *Estuarine and Coastal Mar. Sci.* **9**, 17-27 (1979).

Garrett, C.J.R., J.R.Keeley, D.A.Greenberg. Tidal mixing versus thermal stratification in the Bay of Fundy and Gulf of Maine. *Atmosphere-Ocean* **16**, 403-423 (1978).

Garrett, C.J.R. and J.W. Loder. Dynamical aspects of shallow sea fronts. *Phil. Trans. R. Soc. London* **A:302**, 563-581 (1981).

Greenberg, D.A. A numerical model investigation of tidal phenomena in the Bay of Fundy and the Gulf of Maine. *Mar. Geodesy* **2**, 161-187 (1979).

Greenberg, D.A. Modelling the mean barotropic circulation in the Bay of Fundy and Gulf of Maine. *J. Phys. Oceanogr.* **9**, 886-904 (1983).

Greenberg, D.A. The contribution of modelling to understanding the dynamics of the Bay of Fundy and Gulf of Maine. In *Modelling Marine Systems*, A.M. Davies, ed. CRC Press (in press 1991).

Henry, R.F. Interactive design of irregular triangular grids. In: *Computational Methods in Water Resources, Vol II. Proc. of the VIIth International Conference*, MIT, Cambridge, USA, June 1988. M.A. Celia et al, eds. Computational Mechanics Publications/Elsevier, pp445-450 (1988).

Hukuda, H., R.J. Greatbatch and A.E. Hay. A simple three-dimensional model of the circulation of Newfoundland. *Journal of Geophysical Research*, **94**, 12607-12618 (1989).

Loder, J.W. PhD thesis, Dalhousie University (279 pp), (1980).

Loder, J.W. and D.A. Greenberg. Predicted positions of tidal fronts in the Gulf of Maine region. *Continental Shelf Research* **6**, 3, 397-414 (1986).

Loder, J.W. and D.G. Wright. Tidal rectification and frontal circulation on the sides of Georges Bank. *J. Marine Res.* **43**, 581-604 (1985).

Lynch, D.R. and C.B. Officer. Analytic solutions for three-dimensional hydrodynamic model testing. *Int. J. for Numerical Methods in Fluids.* **5**, 529-543 (1985).

Lynch, D.R. and F.E. Werner. Three-dimensional hydrodynamics on finite elements. Part I: Linearized Harmonic Model. *Int. J. for Numerical Methods in Fluids.* **7**, 871-909 (1987).

Lynch, D.R. and F.E. Werner. Three-dimensional hydrodynamics on finite elements. Part II: Nonlinear time-stepping model. *Int. J. for Numerical Methods in Fluids.* **11** (1990).

Petrie, B., B.J. Topliss, D.G. Wright. Coastal upwelling and eddy development off Nova Scotia. *J. Geophys. Res.* **29**, 12,979-12,991 (1987).

Ramp, S.R., R.J. Schlitz, W.R. Wright. The deep flow through the Northeast Channel, Gulf of Maine. *J. Phys. Oceanogr.* **15**, 1790-1808 (1985).

Simpson, J.H. and J.R.Hunter. Fronts in the Irish Sea. *Nature, London* **250**, 404-406 (1974).

Simpson, J.H. The shelf-sea fronts: implications of their existence and behaviour. *Phil. Trans. R. Soc. London* **A:302**, 531-546 (1981).

Smith, P.C. Seasonal and interannual variability of current, temperature, and salinity off southwest Nova Scotia. *Can. J. Fish. Aquat. Sci.* **46** (Suppl. 1), 4-20 (1989).

Wright, D.G., D.A. Greenberg, J.W. Loder, P.C. Smith. The steady state barotropic response of the Gulf of Maine and adjacent regions to surface wind stress. *J. Phys. Oceanogr.* bf 16, 5, 947-966 (1986).

LIST OF FIGURES

Figure 1a. Idealized tidal front density field (equations 42, 43). From Loder (1980).

Figure 1b. 50 km x 25 km mesh and boundary conditions for the analytic tidal front problem.

Figure 2. Comparison of numerical (solid line) and analytic (circles) baroclinic solutons for idealized tidal front. Analytic solution is from Garrett and Loder (1981). Normalized (a) cross-front and (b) along-front velocities are plotted versus normalized depth. $E \equiv \frac{N}{fh^2} = 0.01$; $\lambda \equiv \frac{N}{kh} = \sqrt{E}$; $s = 0$; 20 vertical elements.

Figure 3. Same as Fig. 2 except $E = .001$. $\lambda = \sqrt{E}$; $s = 0$; 20 vertical elements. The bottom boundary layer is underresolved. (a) cross-front and (b) along-front velocities.

Figure 4. Same as Fig. 3 except the vertical resolution is increased to 100 elements. $E = .001$; $\lambda = \sqrt{E}$; $s = 0$. Accuracy in the bottom boundary layer is restored. (a) cross-front and (b) along-front velocities.

Figure 5. Same as Fig. 2 except $E = 0.1$. $\lambda = \sqrt{E}$; $s = 0$; 20 vertical elements. Note the barotropic error in the along-front velocity, and the loss of the analytic property $V = \frac{\partial V}{\partial z} = 0$ at the bottom. (a) cross-front and (b) along-front velocities.

Figure 6. Same as Fig. 5 except the horizontal resolution is doubled. $E = 0.1$. $\lambda = \sqrt{E}$; $s = 0$; 20 vertical elements. The barotropic error is removed. (a) cross-front and (b) along-front velocities.

Figure 7. Cross-front transect showing vertical and cross-front velocities. Vertical distortion by 500; $s = 0.0$; $L = 30\,km$; $E = .01$; $k = .00125\,m/s$; $\lambda = .07559$.

Figure 8. Cross-front transect showing vertical and cross-front velocities as in Garrett and Loder (1981), in the presence of idealized bank topography. Note the double-gyre structure and convergence of surface velocities. Vertical distortion by 500. $s = 0.5$; $L = 30\,km$; N and k are constant with $E = .01$ at the deep end and $k = .00125\,m/s$.

Figure 9. Location map for the Gulf of Maine region.

Figure 10. Finite element mesh with 3156 nodes and 5558 triangular elements.

Figure 11. Elevation response (cm) to barotropic Scotian Shelf inflow.

Figure 12. Response to Scotian Shelf inflow. (a) vertically averaged velocity, (b) near-bottom velocity. Bathymetric contours are given in meters.

Figure 13. Response to uniform along-shelf wind with 10cm exponential setdown across the Scotian Shelf. (a) vertically averaged velocity, (b) surface velocity, (c) near-bottom velocity.

Figure 14. Map of Georges Bank region showing polygons used in density field preparation and bathymetry.

Figure 15. Vertical structure of summer density on Georges Bank. The transect is from South (left) to North (right) near $67^o W$. Density units are σ_t; distance, km; depth, m.

Figure 16. Vertical density difference in σ_t units, between the surface and $50\,m$ (or bottom where shallower) on Georges Bank from the averaged July-September dataset. The location of the tidal front, taken as $0.2 \leq \Delta\sigma_t \leq 1.5$, is also shown.

Figure 17. Computed response for summer density distribution. (a) surface elevation (cm); (b) surface velocity.

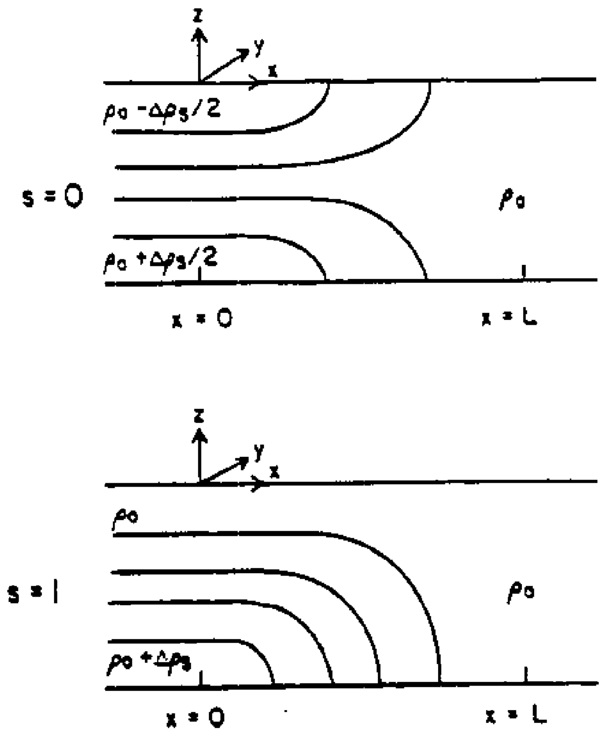

Figure 1a. Idealized tidal front density field (equations 42, 43). From Loder (1980).

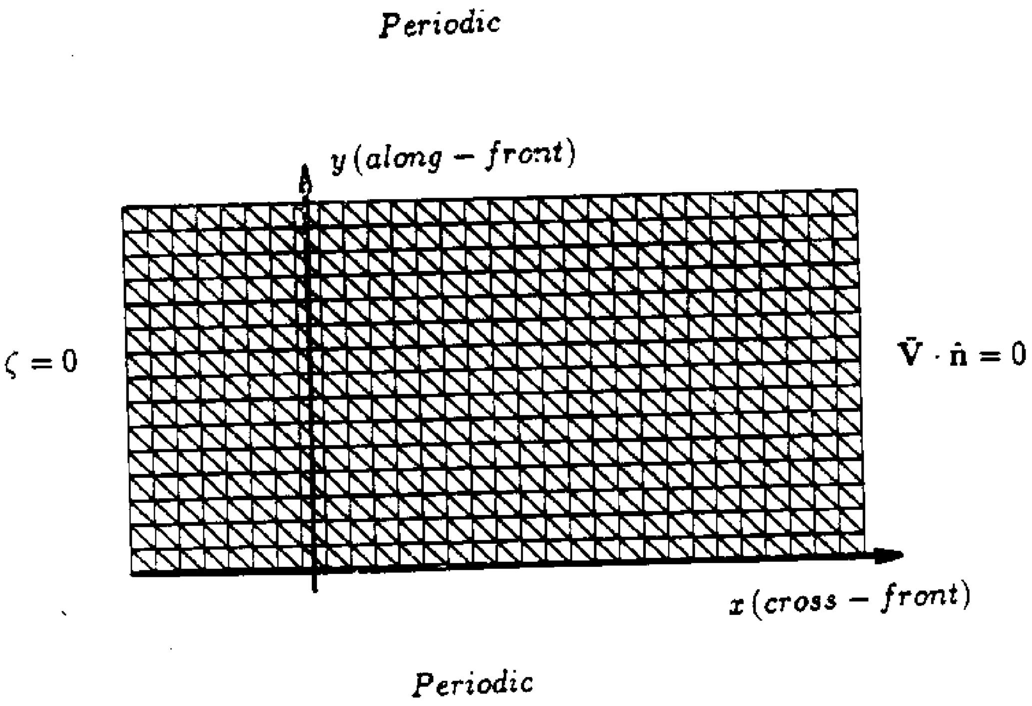

Figure 1b. $50\,km \times 25\,km$ mesh and boundary conditions for the analytic tidal front problem.

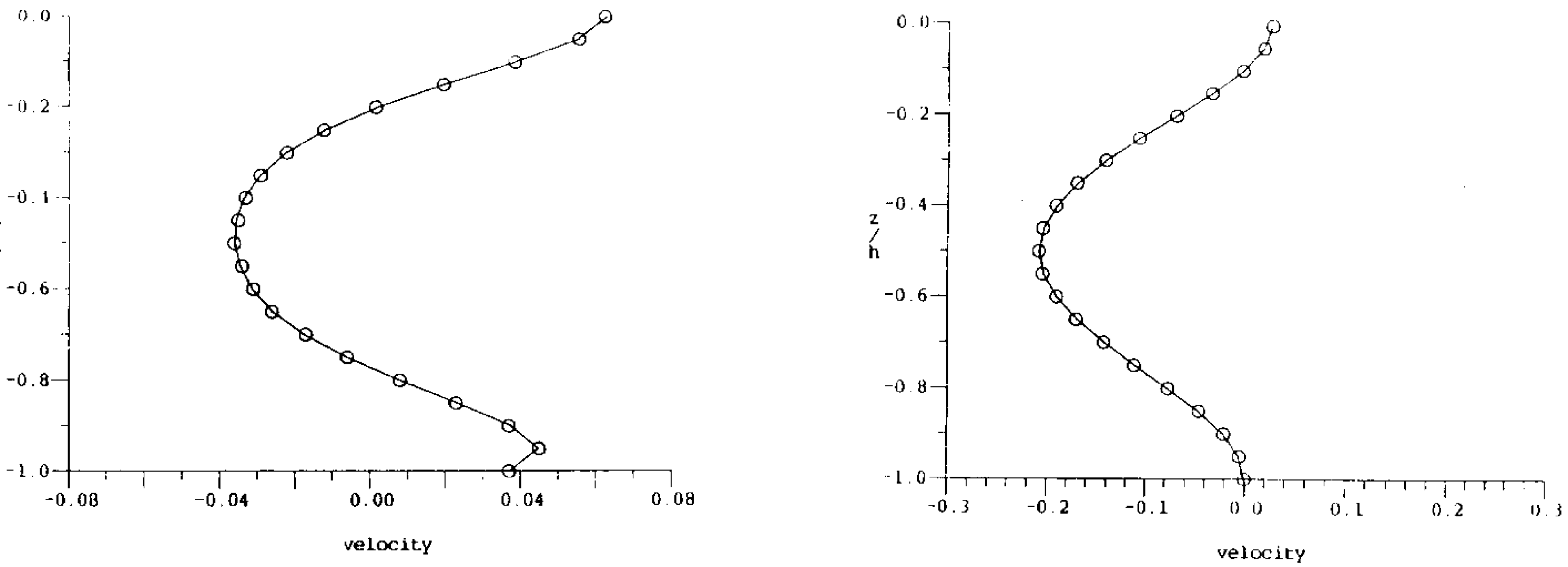

Figure 2. Comparison of numerical (solid line) and analytic (circles) baroclinic solutons for idealized tidal front. Analytic solution is from Garrett and Loder (1981). Normalized (a) cross-front and (b) along-front velocities are plotted versus normalized depth. $E \equiv \frac{N}{fh^2} = 0.01$; $\lambda \equiv \frac{N}{kh} = \sqrt{E}$; $s = 0$; 20 vertical elements.

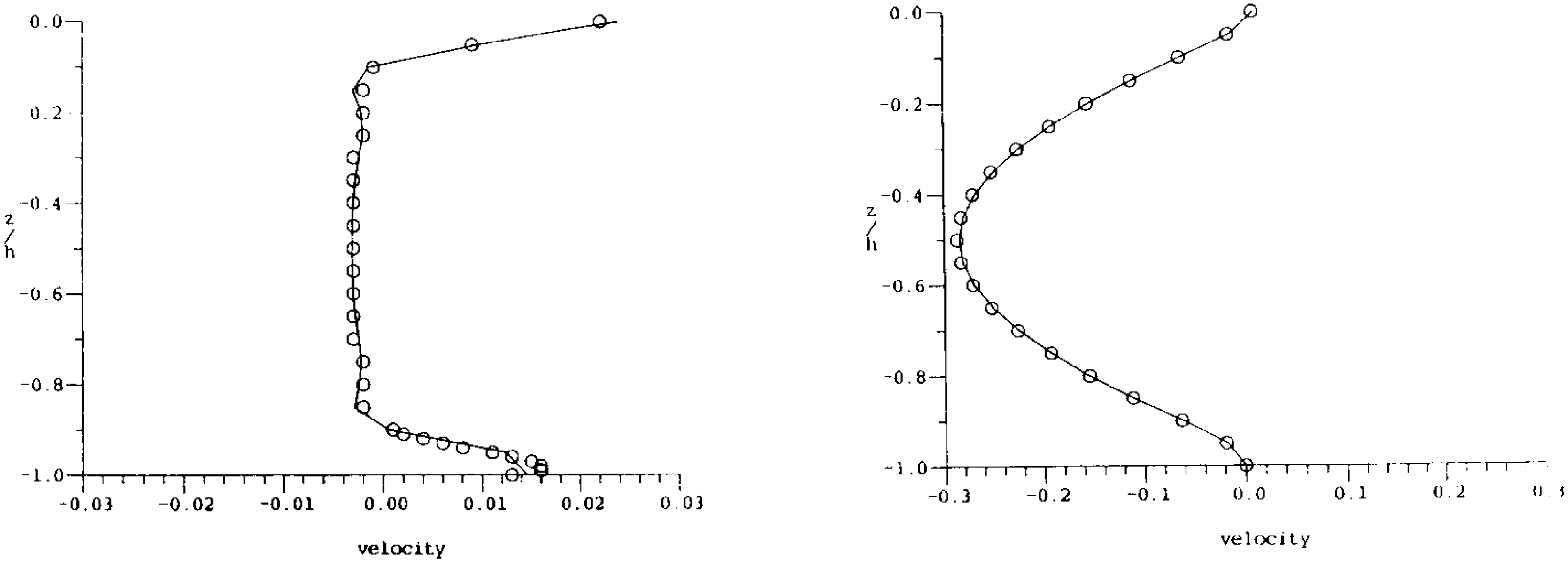

Figure 3. Same as Fig. 2 except $E = .001$. $\lambda = \sqrt{E}$; $s = 0$; 20 vertical elements. The bottom boundary layer is underresolved. (a) cross-front and (b) along-front velocities.

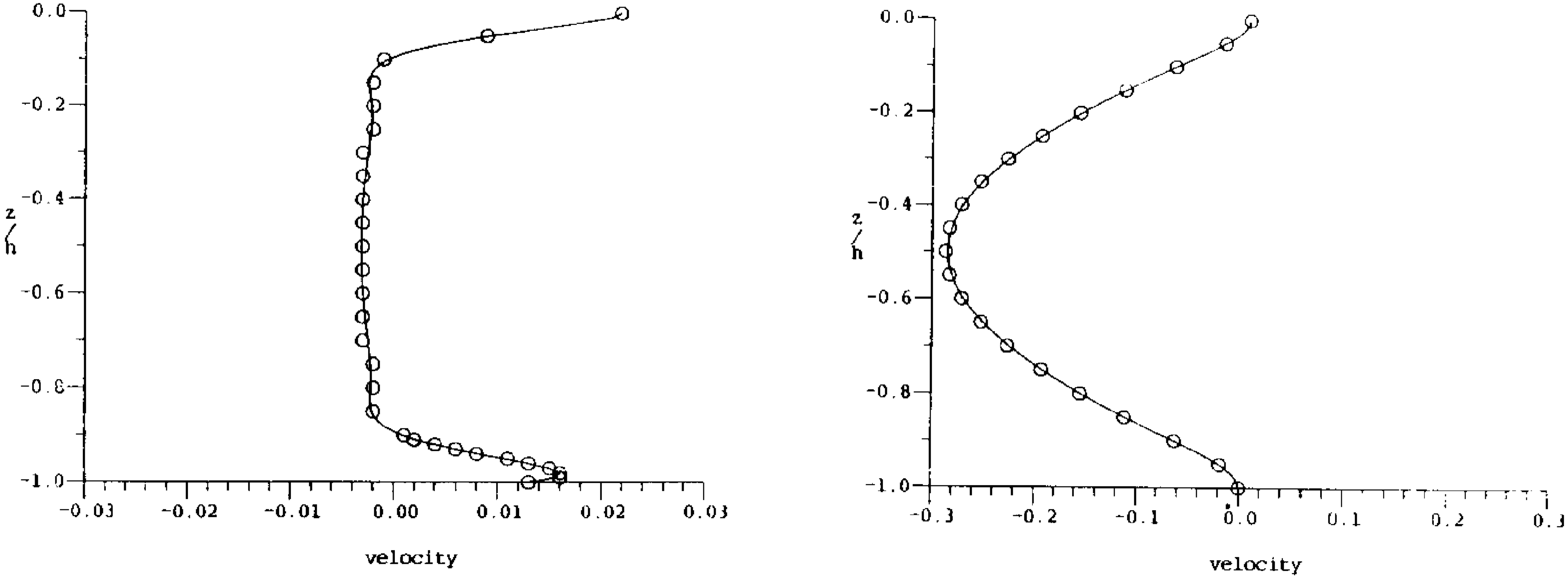

Figure 4. Same as Fig. 3 except the vertical resolution is increased to 100 elements. $E = .001$; $\lambda = \sqrt{E}$; $s = 0$. Accuracy in the bottom boundary layer is restored. (a) cross-front and (b) along-front velocities.

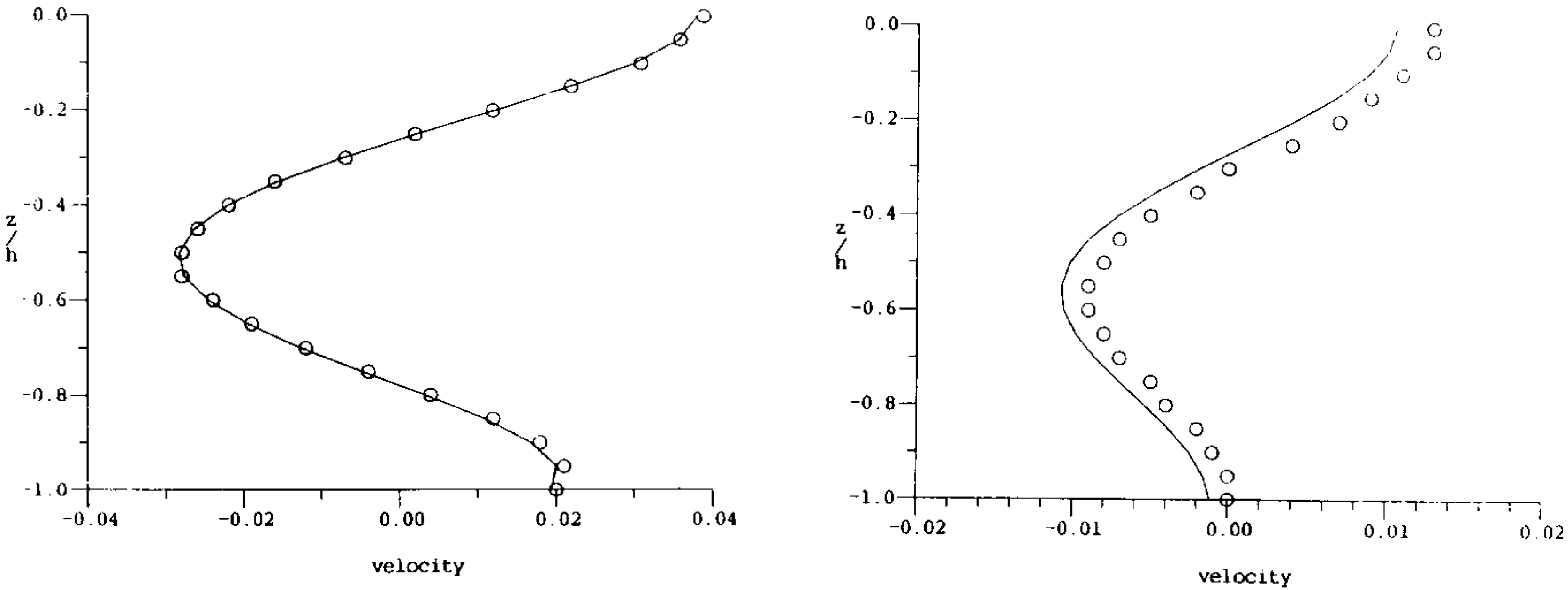

Figure 5. Same as Fig. 2 except $E = 0.1$. $\lambda = \sqrt{E}$; $s = 0$; 20 vertical elements. Note the barotropic error in the along-front velocity, and the loss of the analytic property $V = \frac{\partial V}{\partial z} = 0$ at the bottom. (a) cross-front and (b) along-front velocities.

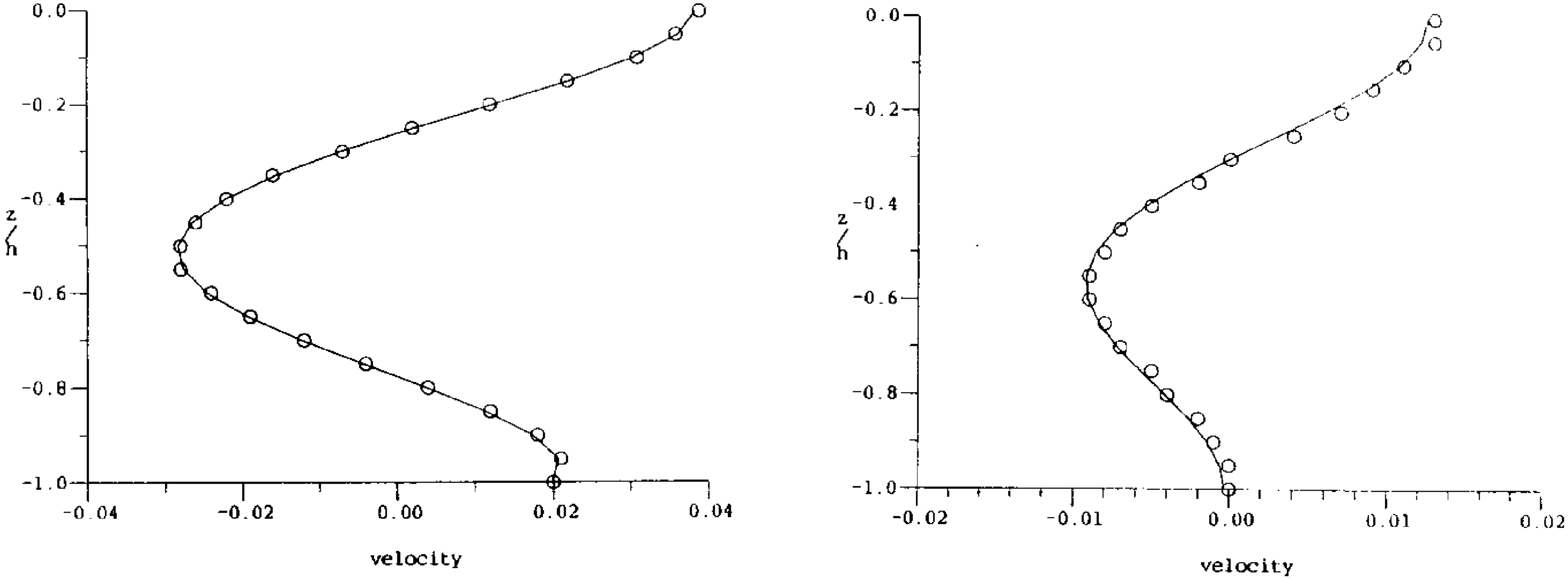

Figure 6. Same as Fig. 5 except the horizontal resolution is doubled. $E = 0.1$. $\lambda = \sqrt{E}$; $s = 0$; 20 vertical elements. The barotropic error is removed. (a) cross-front and (b) along-front velocities.

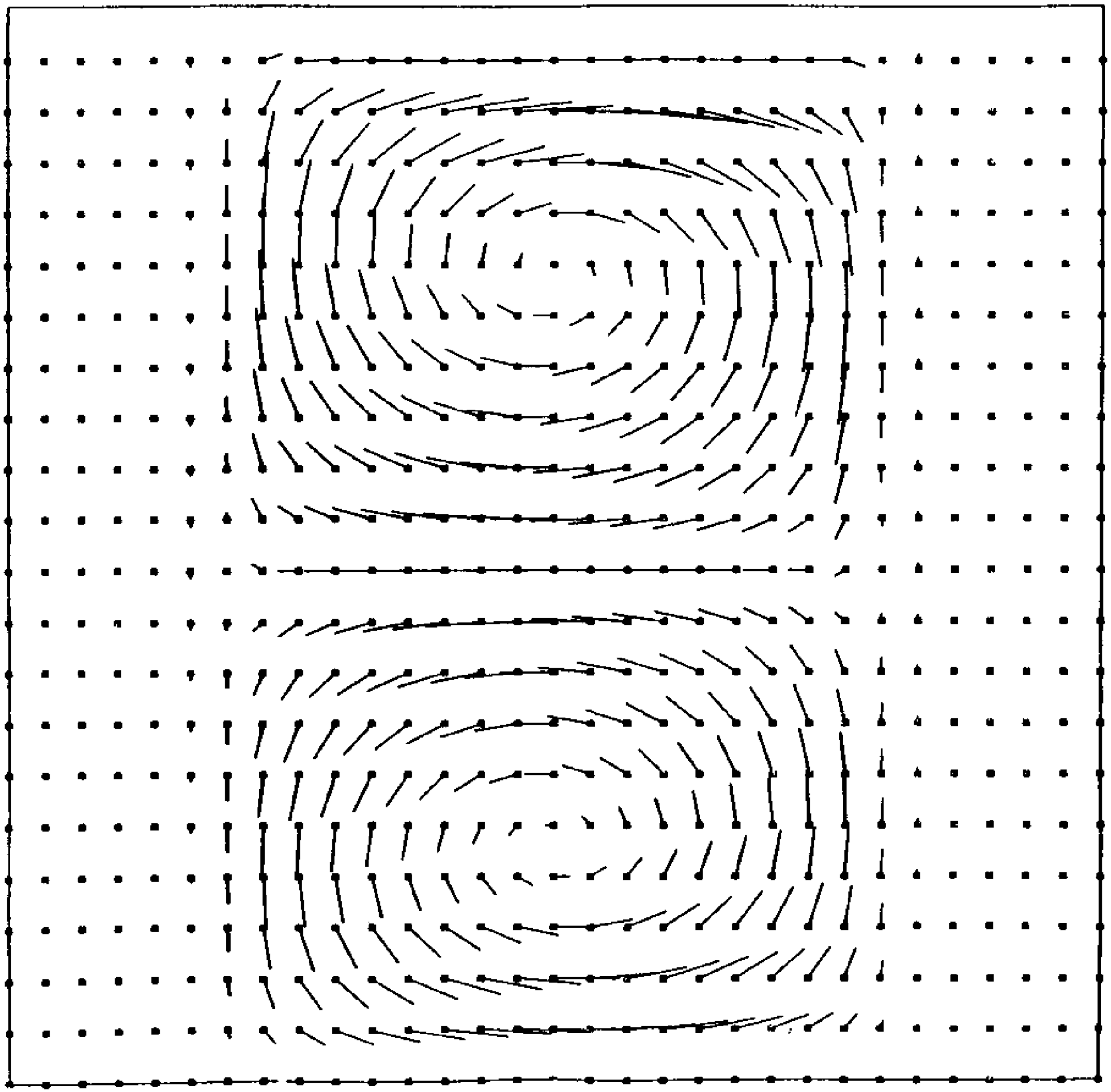

Figure 7. Cross-front transect showing vertical and cross-front velocities. Vertical distortion by 500; $s = 0.0$; $L = 30\,km$; $E = .01$; $k = .00125\,m/s$; $\lambda = .07559$.

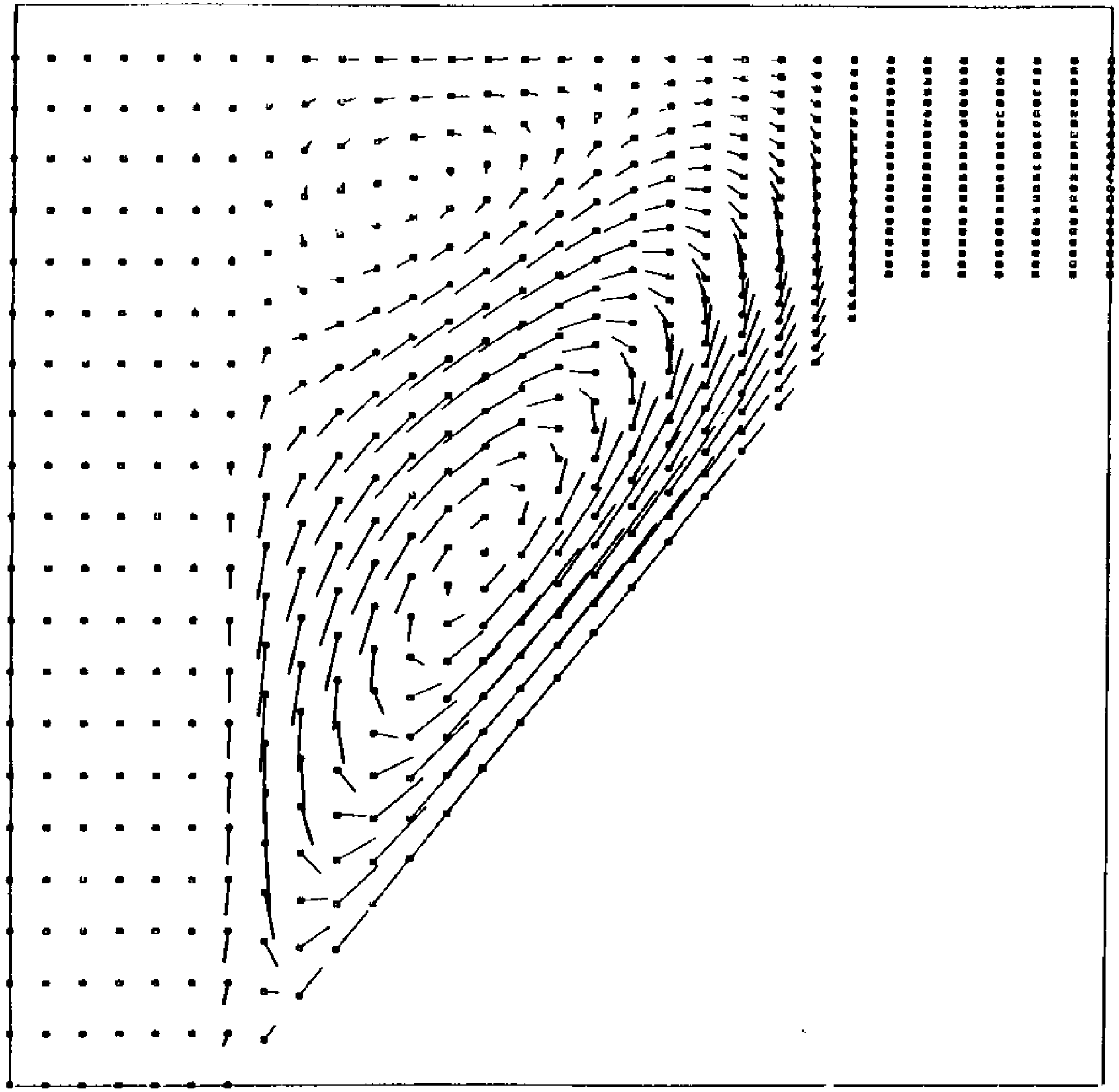

Figure 8. Cross-front transect showing vertical and cross-front velocities as in Garrett and Loder (1981), in the presence of idealized bank topography. Note the double-gyre structure and convergence of surface velocities. Vertical distortion by 500. $s = 0.5$; $L = 30\,km$; N and k are constant with $E = .01$ at the deep end and $k = .00125\,m/s$.

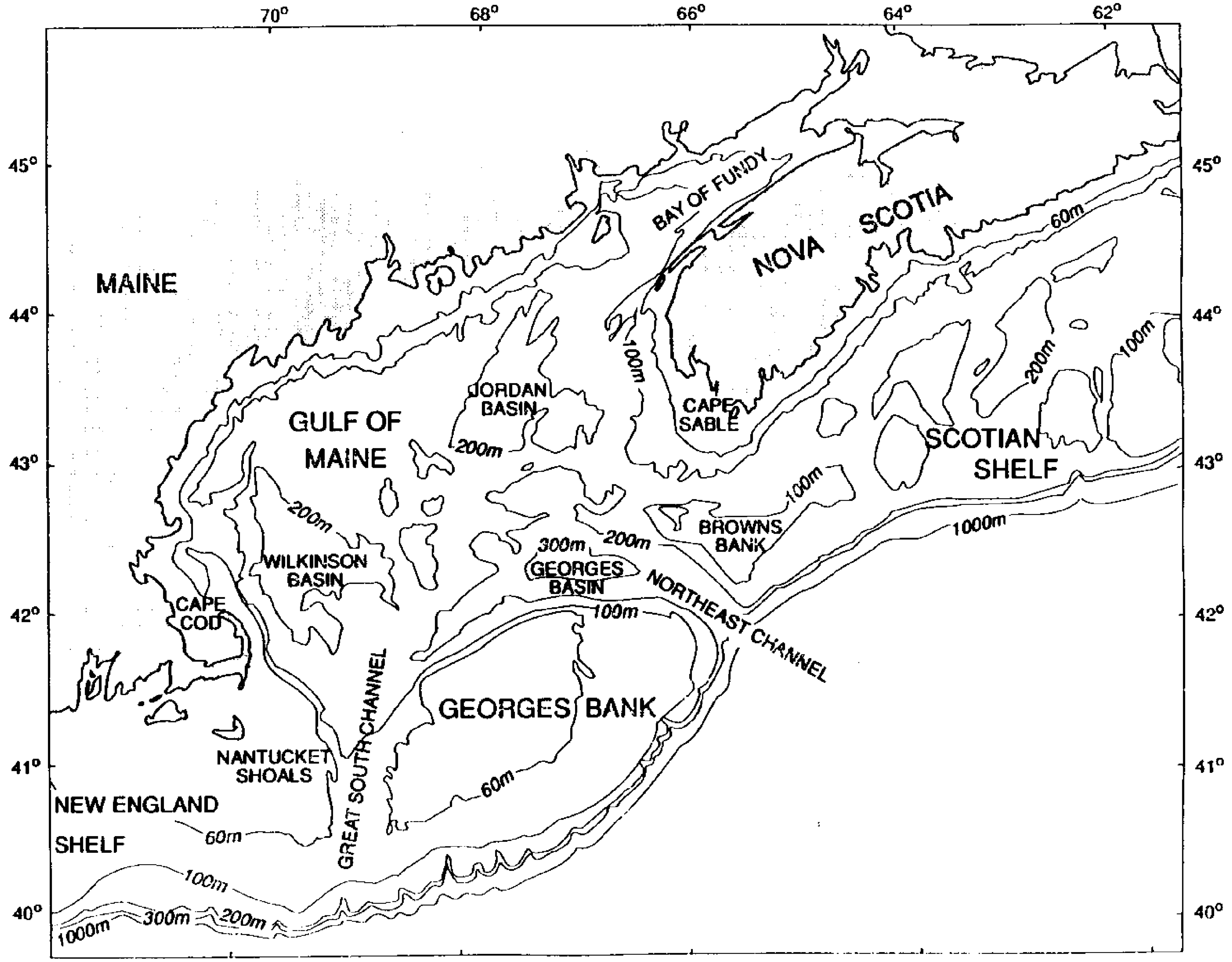

Figure 9. Location map for the Gulf of Maine region.

0076/372/91/3/1

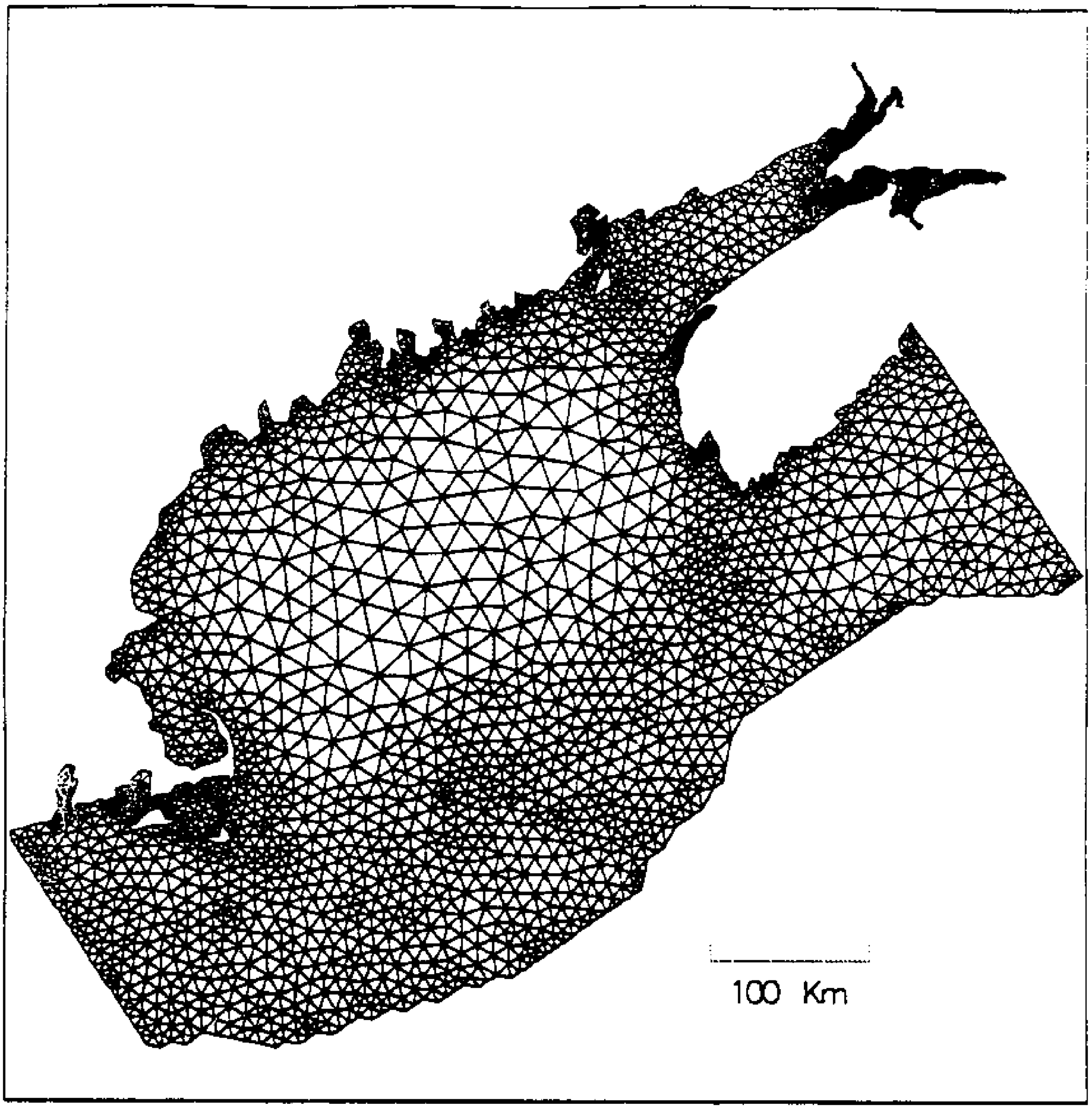

Figure 10. Finite element mesh with 3156 nodes and 5558 triangular elements.

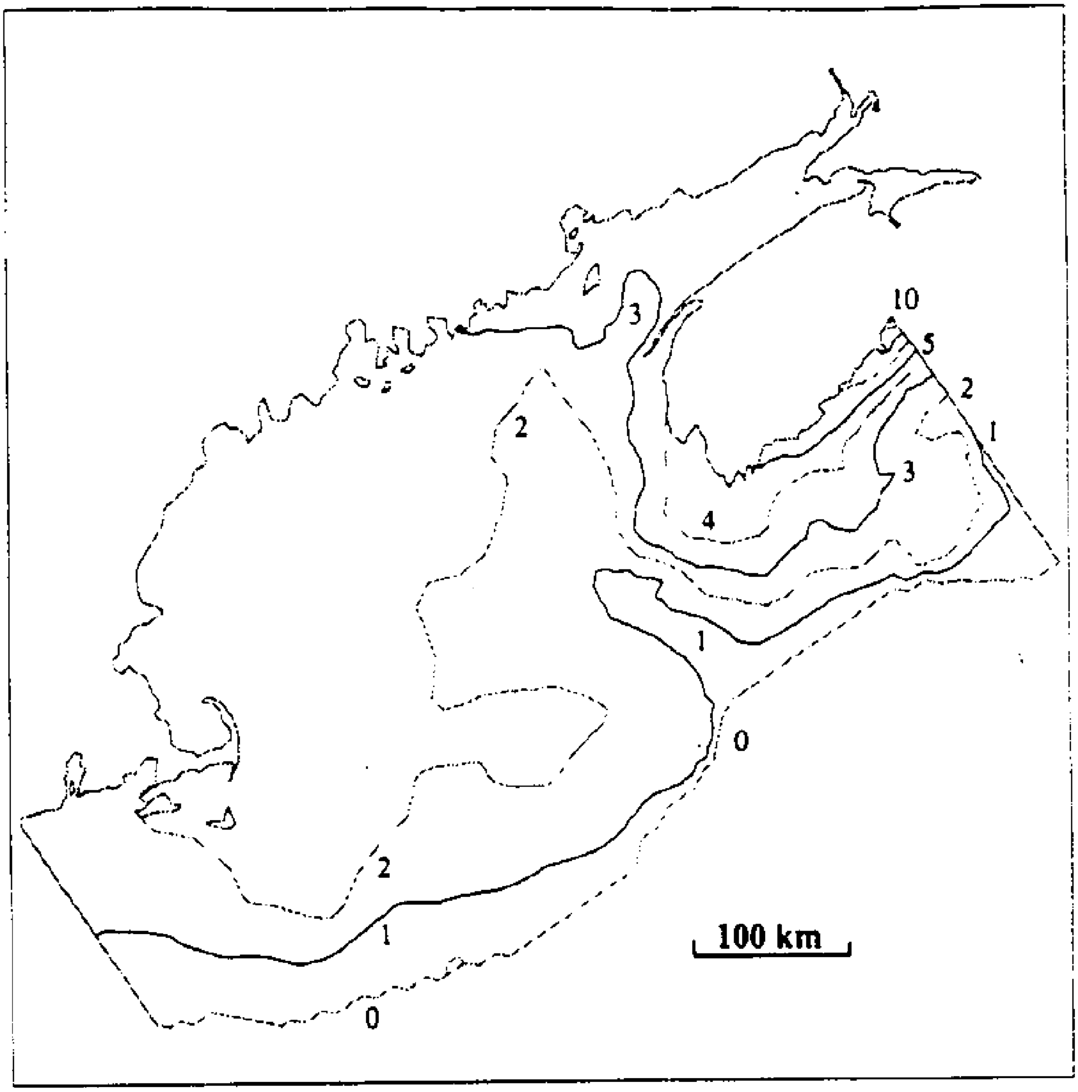

Figure 11. Elevation response (*cm*) to barotropic Scotian Shelf inflow.

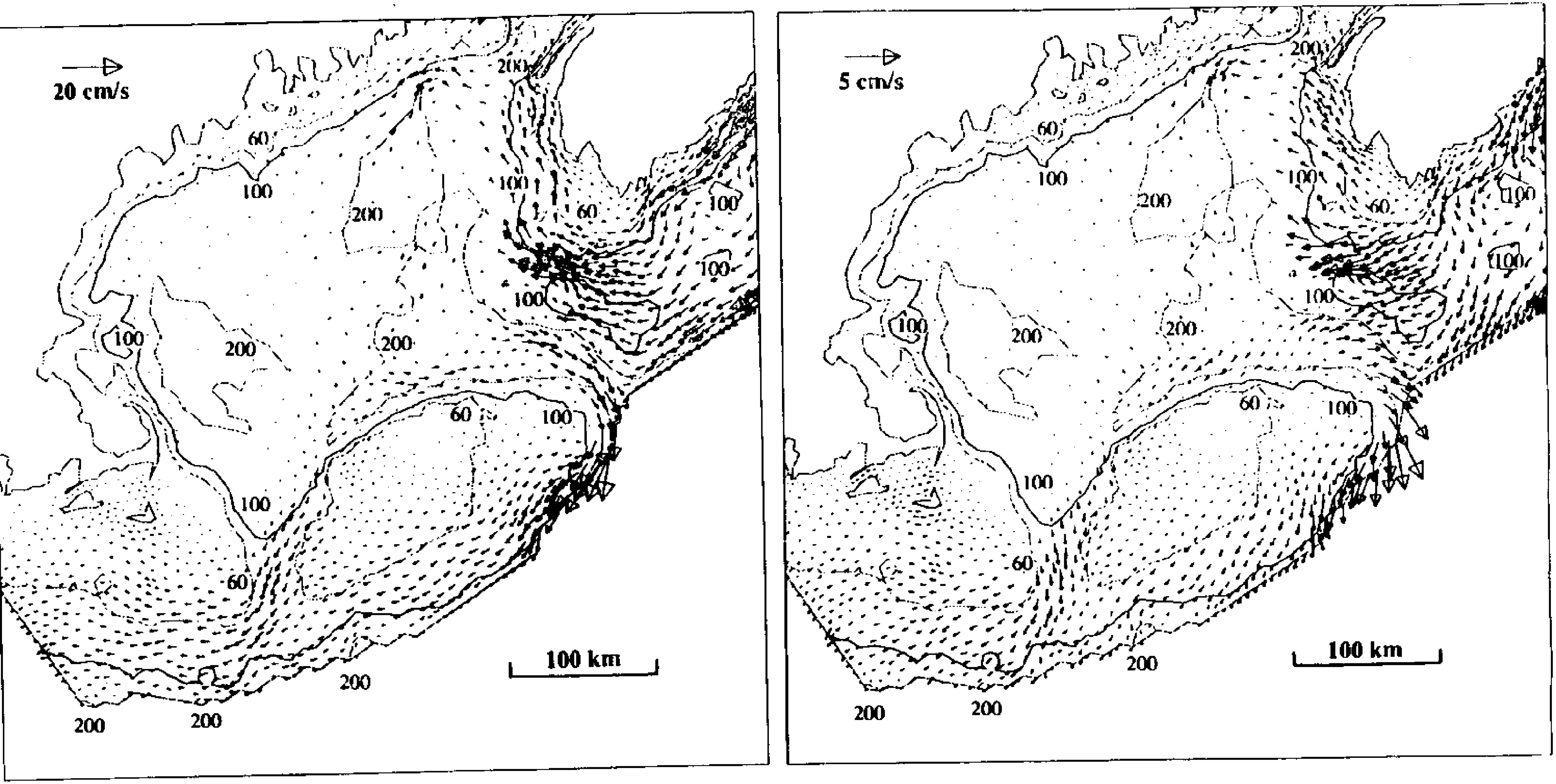

Figure 12. Response to Scotian Shelf inflow. (a) vertically averaged velocity, (b) near-bottom velocity. Bathymetric contours are given in meters.

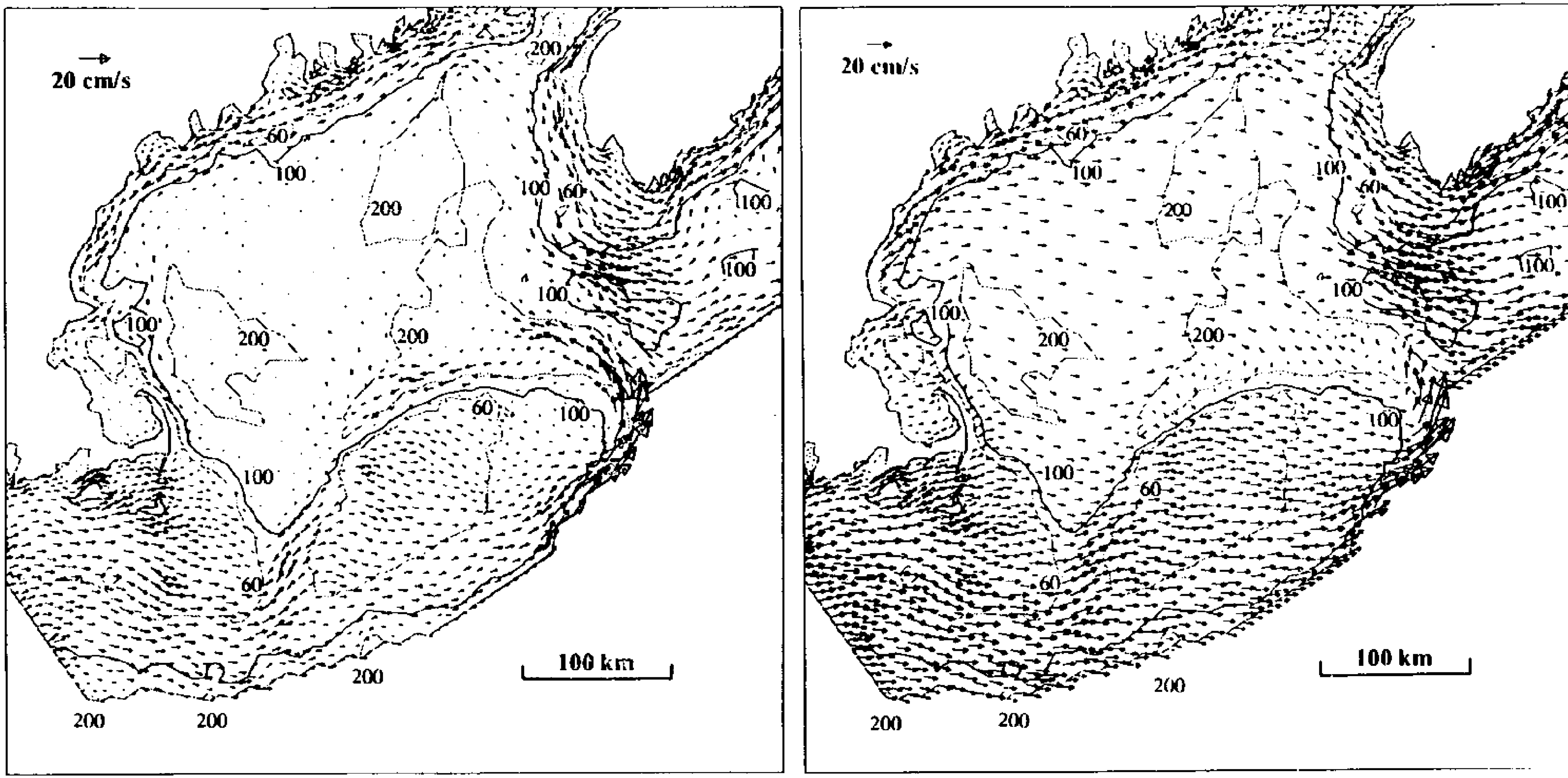

Figure 13. Response to uniform along-shelf wind with 10*cm* exponential setdown across the Scotian Shelf. (a) vertically averaged velocity, (b) surface velocity, (c) near-bottom velocity.

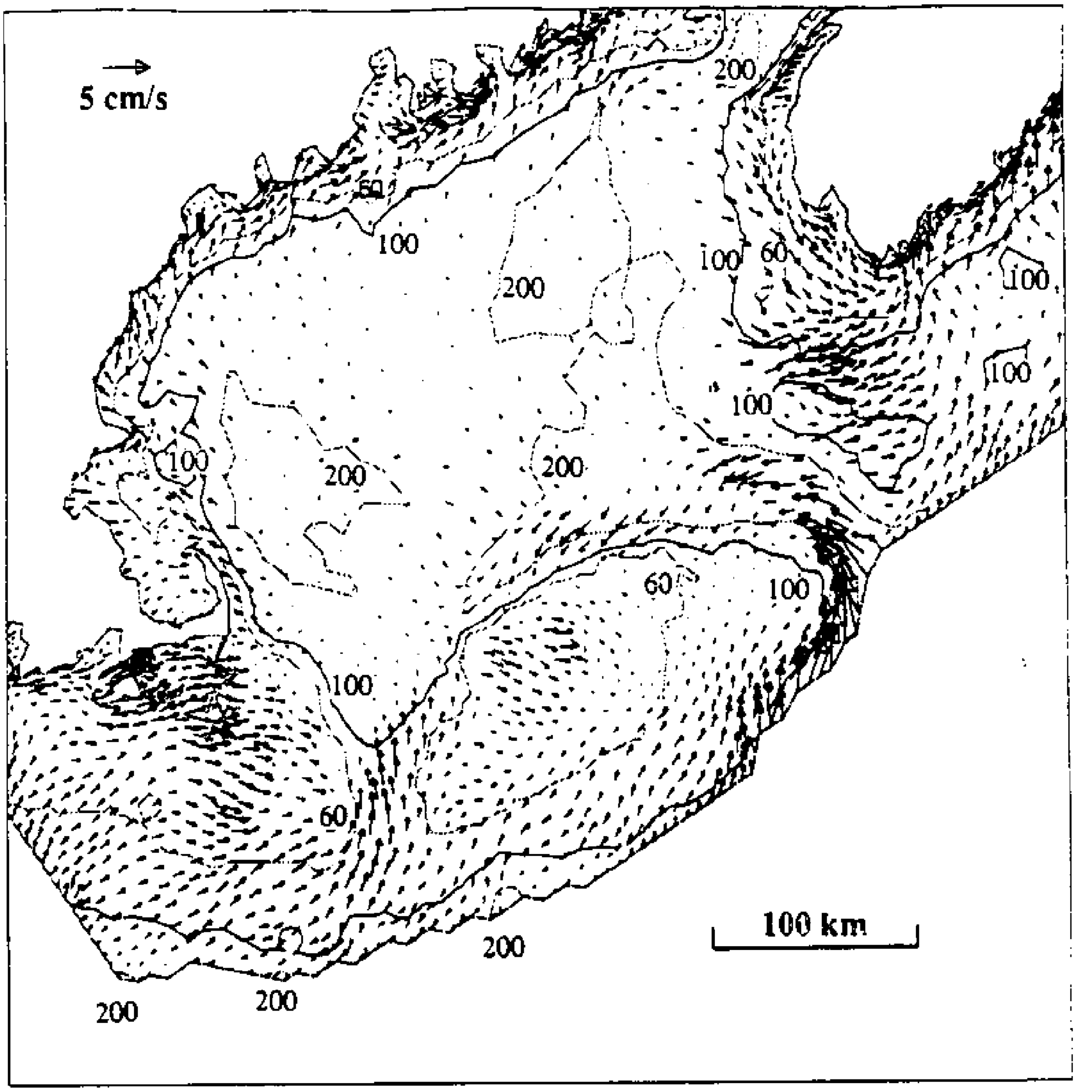

Figure 13c Wind-driven bottom velocity

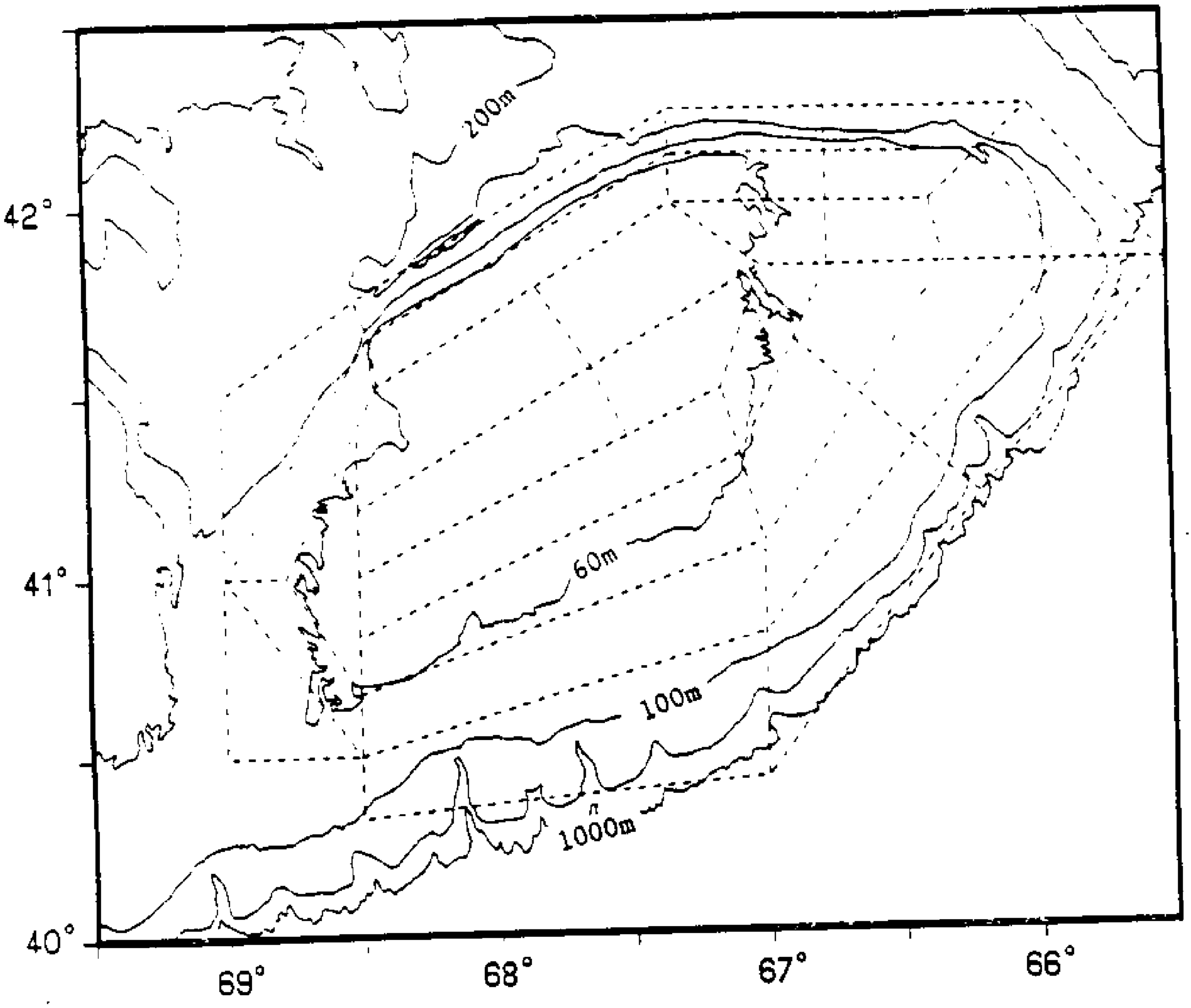

Figure 14. Map of Georges Bank region showing polygons used in density field preparation and bathymetry.

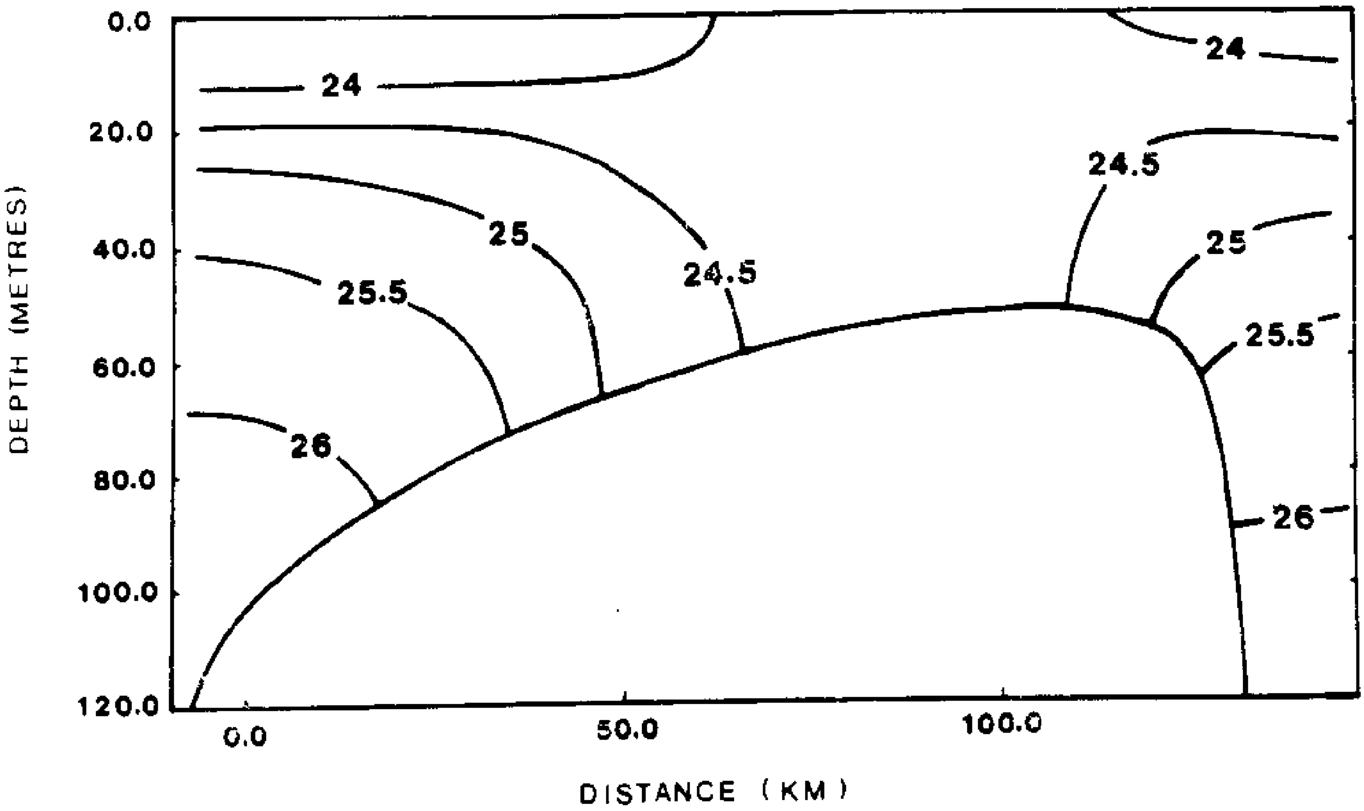

Figure 15. Vertical structure of summer density on Georges Bank. The transect is from South (left) to North (right) near 67° *W*. Density units are σ_t; distance, *km*; depth, *m*.

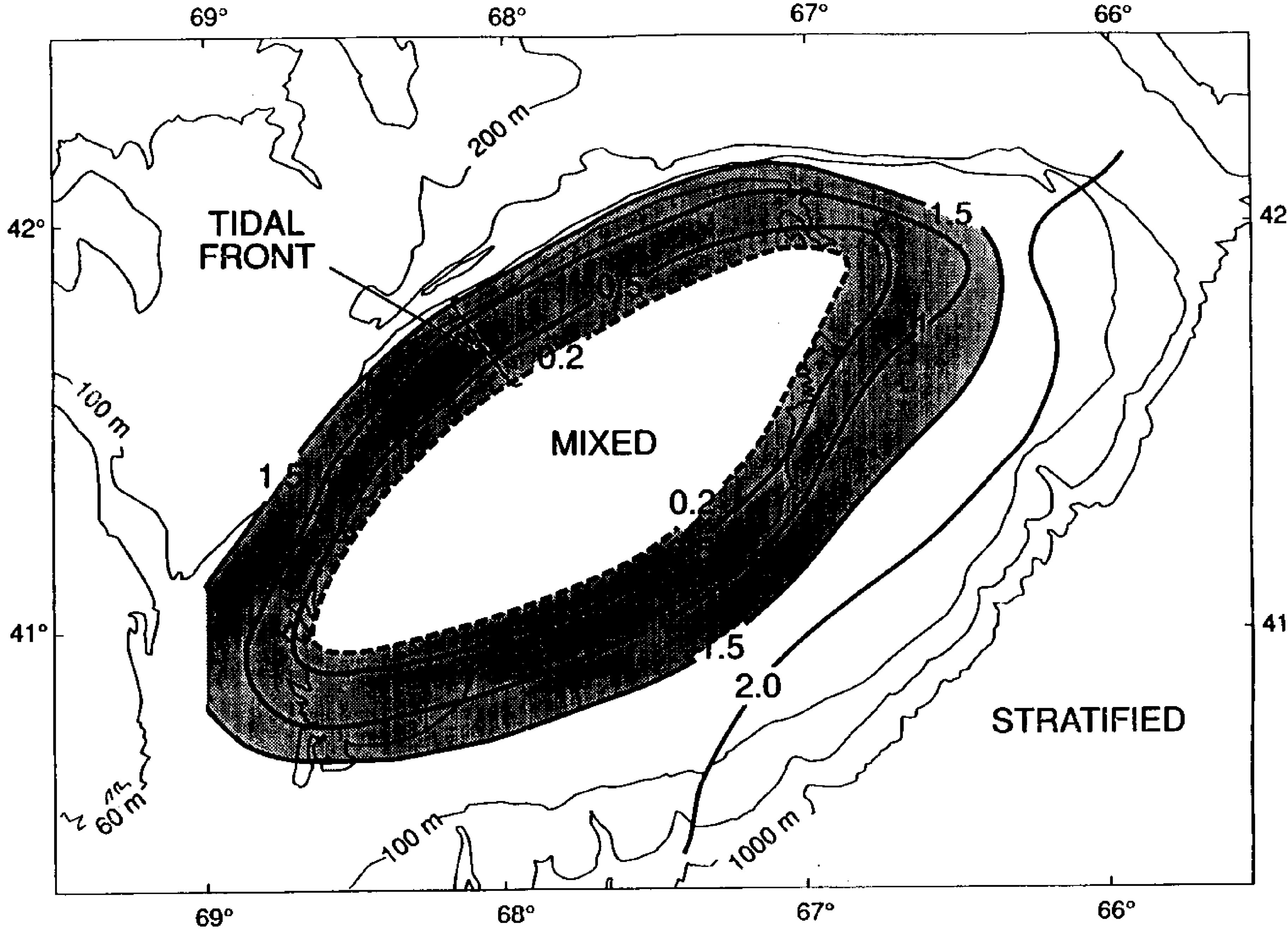

Figure 16. Vertical density difference in σ_t units, between the surface and $50\,m$ (or bottom where shallower) on Georges Bank from the averaged July-September dataset. The location of the tidal front, taken as $0.2 \leq \Delta\sigma_t \leq 1.5$, is also shown.

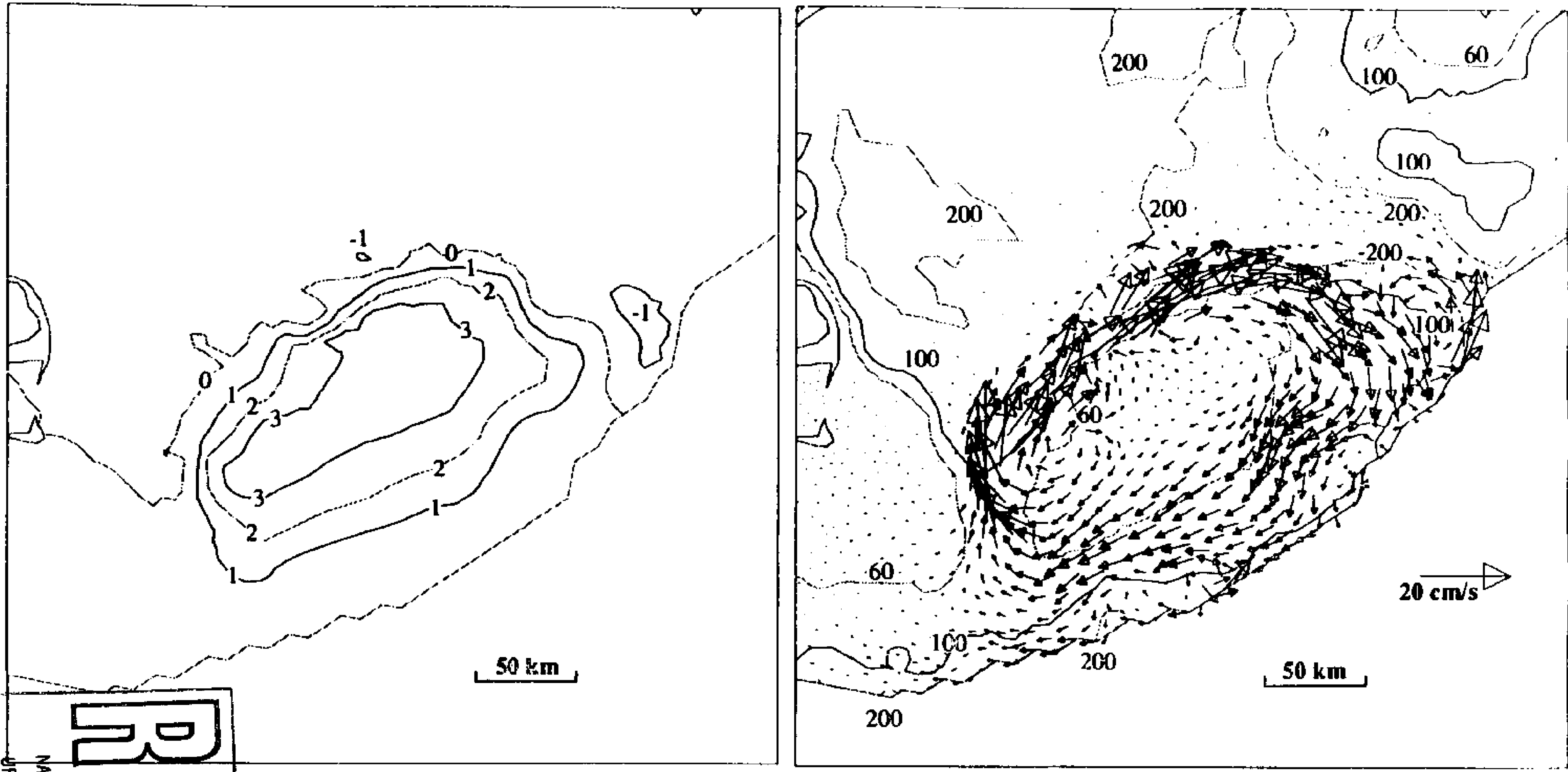

Figure 17. Computed response for summer density distribution. (a) surface elevation (cm); (b) surface velocity.